CONF-7805211--

COO-3904-1

COO-3904-1--10

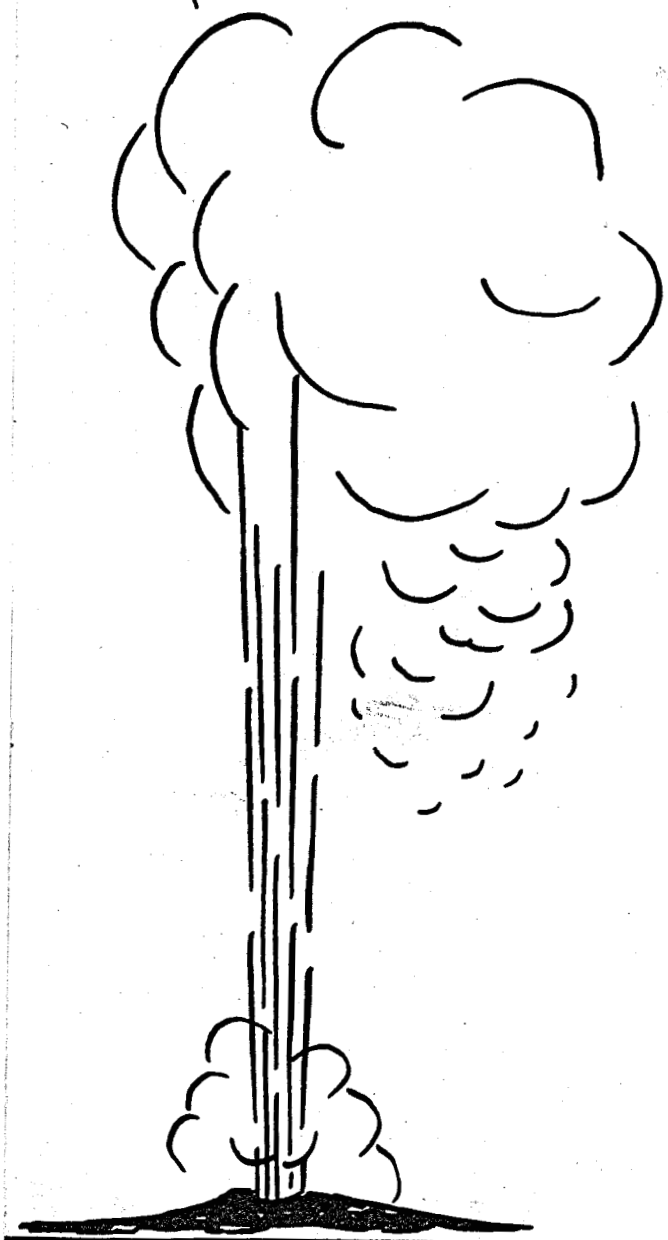

GEOTHERMAL SYSTEMS MATERIALS: A WORKSHOP/SYMPOSIUM

Proceedings, May 23—25, 1978

Work Performed Under Contract No. EG-77-C-04-3904

Radian Corporation
Austin, Texas

U. S. DEPARTMENT OF ENERGY
Geothermal Energy

A THERMODYNAMIC ANALYSIS OF CORROSION PHENOMENA IN HIGH SALINITY GEOTHERMAL BRINES

By

Digby D. Macdonald and Barry C. Syrett

Materials Research Center
SRI International
Menlo Park, California 94025

DISCLAIMER

INTRODUCTION

It is well recognized that high-salinity geothermal environments are corrosive to many metals and alloys.[1-4] The high corrosiveness of the environment arises from the combination of elevated temperature (e.g., up to 350 C), and the presence of a high concentration of chloride ion (typically up to 4 m). Hydrogen sulfide is also frequently present, although usually only in the parts-per-million concentration range. Nevertheless, sulfide attack might be expected on many of the materials of technical interest. Furthermore, the related sulfide-induced failure mechanisms may also impose severe limits on the use of high strength alloys in geothermal systems, as has been the case in the sour natural gas industry. Accordingly, a major factor in the economic exploitation of geothermal resources will be the cost-effective selection of materials that have sufficient resistance to corrosion to maintain component integrity.

In this paper we review our recent studies[2-4] of the corrosion potential and cyclic voltammetric behavior of AISI 1010 carbon steel, E-Brite 26-1 stainless steel, AISI 316L stainless steel, Haynes Alloy 20 Mod, Carpenter 20 Cb-3, Inconel Alloy 625, Hastelloy Alloy G, Hastelloy Alloy C-276, Titanium 50A (ASTM B265 Gr. 2), and TiCode 21 in a sulfide-free high-salinity geothermal brine taken from a producing well located in the

Imperial Valley in Southern California. Potential-pH diagrams for the component metal (Fe, Ni, Cr, Ti)-brine systems[2,3] at temperatures of 25°C and 250°C are used to rationalize the corrosion potentials and the oxidation and reduction peak potentials for the alloys observed by cyclic voltammetry.[5] Previous work[6-8] has shown that comparison of experimental corrosion and cyclic voltammetric peak potentials with calculated equilibrium potentials is a useful method for analyzing the corrosion behavior of metals and alloys in aqueous systems at elevated temperature.

We also report potential-pH diagrams for iron and nickel in high salinity brine at 25°C and 250°C containing 10 ppm of total dissolved sulfide.[2,4] These diagrams are used to analyze the general features of the thermodynamic behavior of iron and nickel in high temperature sulfide-containing geothermal systems.[4]

EXPERIMENTAL

Corrosion potentials and cyclic voltammograms were measured using a conventional once-through flow line containing a 2-liter pressure vessel manufactured from Hastelooy Alloy C-276. The design and operation of the apparatus have been fully described elsewhere.[2]

The brine used was taken from the Magmamax No. 1 well near Niland, California, and was reconstituted by sparging with a N_2 + 2 vol% CO_2

gas mixture to adjust the pH to the wellhead value (at ambient temperature) of 5.2. The chemical composition of the brine used for the experimental work in this study is given in Table 1.[2] In spite of our attempts[2] to maintain the chemical stability of the brine during transportation and storage, a sludge precipitated over a period of time. Energy dispersive X-ray (EDX) analysis showed that this precipitate contained Fe, Si, Al, Cl, and some Ca, Na, and K. Only NaCl was identified by X-ray diffraction analysis, although two additional, but unindexed, lines were also observed. The halite (NaCl) phase presumably precipitated during drying of the sludge. Further precipitation occurred when the filtrate was stored in a polyethylene bottle that remained open to the atmosphere.

Specimens (1 cm x 1 cm x 0.16 cm) of each alloy were exposed simultaneously to the brine for the determination of the corrosion potentials and acquisition of cyclic voltammograms. The chemical compositions of the alloys are given in Table 2. Each specimen was given an abraded finish with 120-grit SiC paper, and was degreased with acetone, washed with distilled water, and air-dried before exposure to the brine environment.

Cyclic voltammograms[5] were recorded by linearly sweeping the potential for each alloy between the limits given in Table 3. A single sweep rate of 0.010 V/s was used, and the voltammograms were recorded over at least

Table 1

CHEMICAL COMPOSITION OF THE MAGMAMAX No. 1 BRINE USED IN THE LABORATORY TESTS
(Total Dissolved Solids = 215.8 mg/l)

Element	Method	Concentration mg/l
Cl	XRF	129,000
Na	AA	52,000
Ca	XRF	25,000
K	XRF	6,250
Mg	XRF	1,100
P	C	~ 500
Mn	XRF	450
Sr	XRF	360
Zn	XRF	240
Si	AA	190
Fe	XRF	180
Br	XRF	100
Rb	XRF	65
Pb	XRF	46
V	XRF	30
B	PT	25
Al	AA	25
Li	PT	≤ 25
Ba	XRF	< 10
I	XRF	< 10
Ti	XRF	< 10
As	XRF	6.2
F	ISE	< 5.0
Cr	XRF	< 5.0
Cd	XRF	3.7
Co	XRF	< 2.0
Ni	XRF	< 1.5
Cu	XRF	1.4
Sn	XRF	< 1.0
Hg	XRF	< 0.50
Se	XRF	< 0.50
Ag	XRF	0.35

XRF = X-ray fluorescence; AA = atomic absorption; C = colorimetry, PT = potentiometric titration; ISE = ion selective electrode; <5.0 = not detected (limit of detectability is 5.0 mg/l).

Table 2

CHEMICAL COMPOSITIONS OF TEST MATERIALS

(Weight Percent)

Alloy	Fe	Ni	Cr	Co	Mo	W	Si	Mn	C	Cu	Ti	P	S	Other
AISI 1010 Carbon Steel	Bal	-	-	-	-	-	0.01	0.31	0.061	-	-	0.009	0.012	
E-Brite 26-1 Stainless Steel[a]	Bal	0.11	26.01	-	1.01	-	0.22	0.02	< 0.001	0.02	-	0.012	0.011	0.010 N
AISI 316L Stainless Steel[b]	Bal	13.29	17.39	-	2.31	-	0.63	1.79	0.021	-	-	0.021	0.007	
Haynes Alloy 20 Mod[c]	Bal	25.87	21.85	-	4.23	-	0.58	0.84	0.03	-	0.36	0.013	0.010	
Carpenter 20 Cb-3[b]	Bal	33.13	19.35	0.33	2.20	-	0.43	0.26	0.03	3.22	-	0.02	0.002	0.78 Cb + Ta
Inconel Alloy 625[d]	3.10	Bal	21.41	-	8.82	-	0.30	0.11	0.03	-	0.31	0.013	0.002	3.47 Cb + Ta, 0.18 Al
Hastelloy Alloy G[c]	18.98	Bal	21.99	1.82	6.47	0.51	0.32	1.34	.0.03	1.77	-	0.025	0.010	2.11 Cb + Ta
Hastelloy Alloy C-276[c]	5.94	Bal	15.15	2.04	15.48	3.37	0.03	0.40	0.004	-	-	0.013	0.009	0.19 V
Titanium 50A (ASTM B265 Gr.2)[e]	0.13	-	-	-	-	-	-	-	0.013	-	Bal	-	-	0.008 N, 0.004 H, 0.11 O
TiCode 12[e]	0.11	0.84	-	-	0.29	-	-	-	0.012	-	Bal	-	-	0.009 N, 0.14 O

[a]Donated by Airco Vacuum Metals.
[b]Donated by Carpenter Technology Corporation.
[c]Donated by Stellite Division of Cabot Corporation.
[d]Donated by Huntington Alloys Inc.
[e]Donated by Timet.

Table 3

CORROSION POTENTIAL AND CYCLIC VOLTAMMETRIC DATA FOR THE ALLOYS IN HIGH SALINITY BRINE AT 250°C

	E_{corr}	E_{ff}	Polar. Limits	E_p (Oxidation)	E_p (Reduction)
AISI No. 1010 Carbon Steel	-0.66 to -0.45	-0.71 to -0.69	-1.06 to 0.11	(-0.41), -0.36, -0.18	-0.73
E-Brite 26-1	-0.47 to -0.35	-0.89 to -0.80	-1.97 to 1.03	-0.72, -0.62, (-0.48), (-0.05), 0.44	-1.32
316L SS	-0.44 to -0.34	-0.89 to -0.87	-1.99 to 0.46	-0.67, -0.61	
Haynes Alloy 20 Mod	-0.44 to -0.33	-0.95 to -0.80	-1.98 to 0.14	(-0.85), -0.73, -0.55, (-0.42)	
Carpenter 20 Cb-3	-0.42 to -0.32	-0.95 to -0.88	-1.97 to 0.23	-0.88, -0.72, -0.55	
Inconel Alloy 625	-0.44 to -0.33	-0.99 to -0.77	-1.99 to 0.22	-0.95, -0.74, -0.53	-1.20
Hastelloy Alloy G	-0.47 to -0.33	-0.99 to -0.78	-1.97 to 0.13	-0.95, -0.74, -0.57, -0.41 (-0.11)	
Hastelloy Alloy C-276	-0.45 to -0.32	-0.99 to -0.81	-1.98 to 0.31	-0.90, -0.70, -0.52, -0.38	-1.32,-0.97, (-0.79)
Titanium 50A	-0.47 to -0.34	-0.56 to -0.40	-1.99 to 1.04	-0.87, -0.50, -0.22, 0.14, 0.29, 0.56	
TiCode 12	-0.48 to -0.38	-0.73 to -0.45	-1.99 to 1.03	-0.67, -0.61, -0.42, -0.34, -0.17, 0.36, 0.50, 0.85	-1.78

All potentials are in volts versus the standard hydrogen electrode at 250 C.
E_{corr} - Corrosion Potential. E_{ff} - zero current potential after reduction. (-0.41) - brackets around a potential indicate a point of inflection rather than a peak.

three successive cycles. The cyclic voltammograms were measured during the last 50 hours of the test. The specific time of aquisition for each alloy is given in the caption of the appropriate figure (Figs. 3-12). All experiments were carried out at a temperature of 250°C and at a pressure of 5.52 MPa. The pressure, which was sufficiently high to prevent boiling, was maintained by use of a metering pump and a pressure release valve in the outlet leg of the system.

All potential measurements were made with respect to internal silver-silver chloride electrodes[9] (0.1 m KCl or 3.6 m KCl) operating at the temperature of interest, as previously described.[2,3] The higher KCl concentration in one of the reference electrodes was used to minimize the liquid junction potential between the brine (~ 3.6 m KCl) and the electrode contents. In general, the 0.1 m KCl electrode gave more reliable service than that with the 3.6 m KCl electrolyte; a behavior that we attribute to a lower tendency in the dilute system to form soluble silver chloride anionic complexes of the type $AgCl_{n+1}^{2-}$ or possibly due to a lower susceptibility to reduction of silver chloride by dissolved hydrogen.[8,10]

RESULTS

Corrosion Potential

The variation of corrosion potential for each alloy with time from startup at 22°C to termination of the experiment after 150 hours exposure at 250°C is shown in Figs. 1 and 2. For all materials studied,

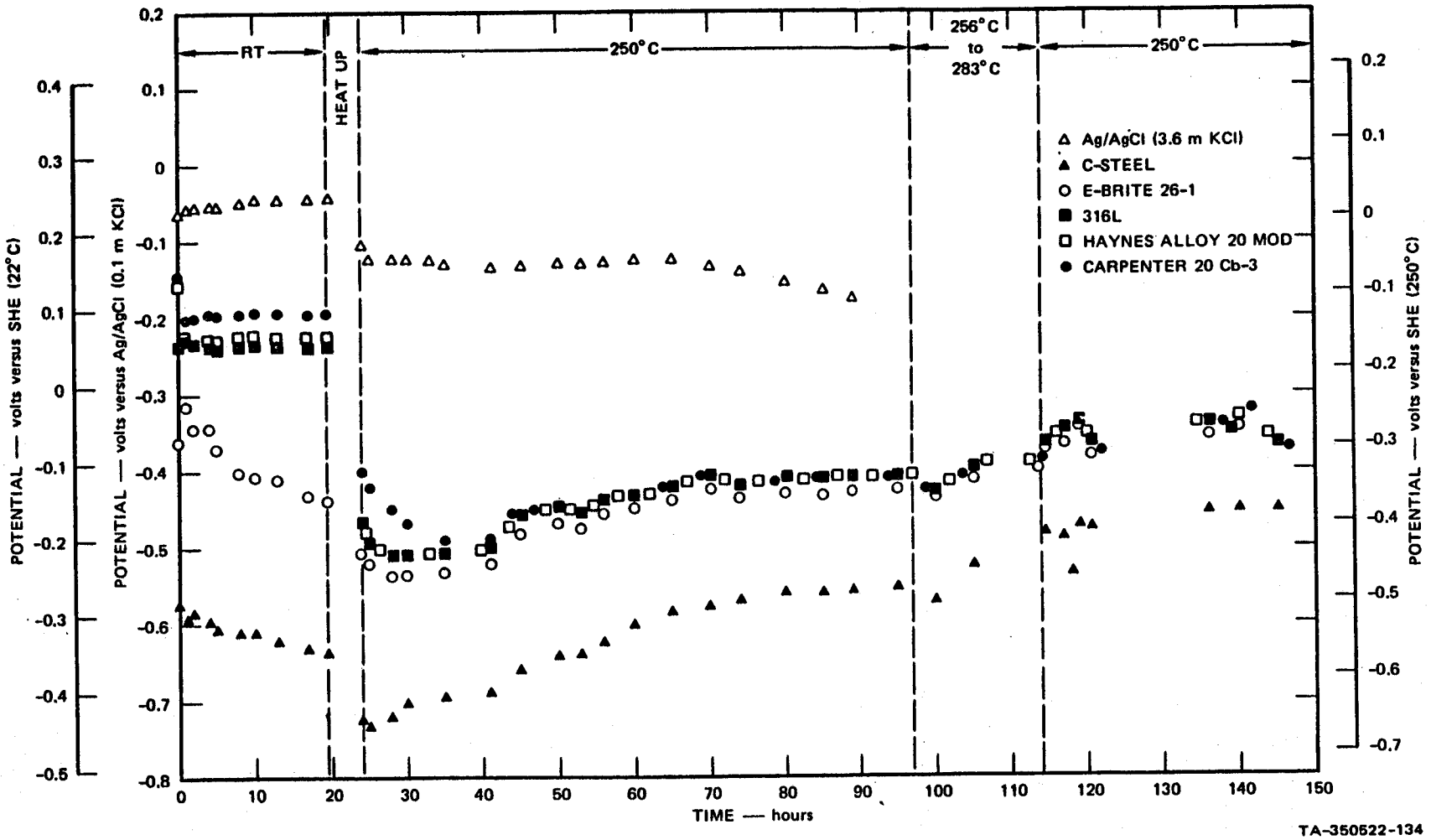

FIGURE 1 CORROSION POTENTIAL-TIME CURVES FOR IRON-BASED MATERIALS IN HIGH-SALINITY BRINE (pH 5.36 AT 25°C)
RT — room temperature

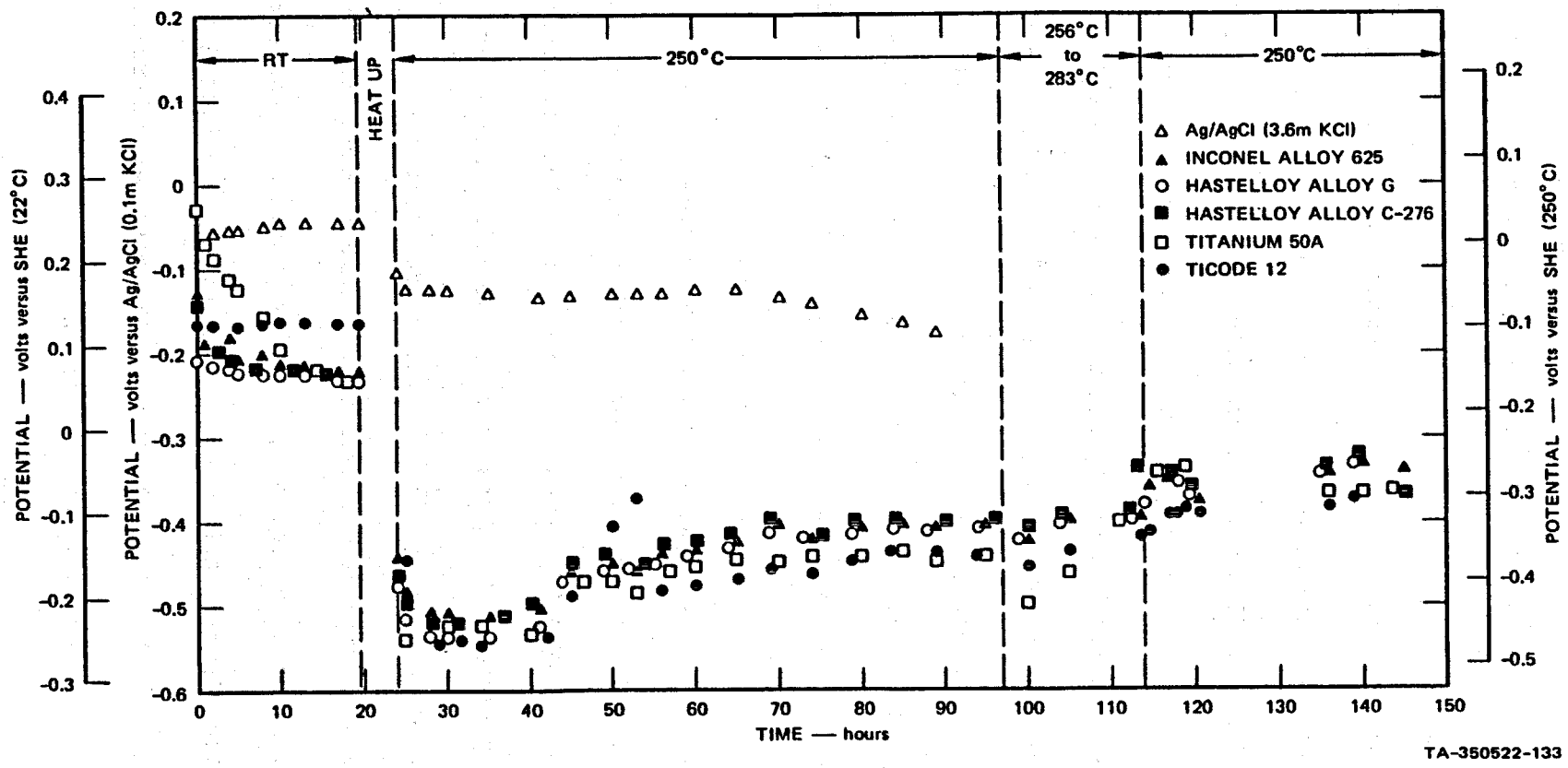

FIGURE 2 CORROSION POTENTIAL-TIME CURVES FOR NICKEL- AND TITANIUM-BASED MATERIALS IN HIGH-SALINITY BRINE (pH 5.36 AT 25°C)

RT — room temperature

the corrosion potential was found to shift sharply to more active values when the temperature of the system was changed from 22°C to 250°C. A gradual drift of E_{corr} with time to more noble values was then observed over the 130-hour exposure period at elevated temperatures. The corrosion potential was not significantly affected by the temperature excursion to 283°C that occurred between 97 and 113 hours after initiation of the test. The sudden change to more active values that occurred when the system was heated parallels the behavior previously observed for carbon steel in lithium hydroxide solution at elevated temperatures.[11] This sudden shift probably reflects the consumption of trace amounts of oxygen in the system as the temperature is changed, and also the tendency for many metals and alloys to corrode in the "active" state in aqueous systems at elevated temperatures.[6-8]

The more negative corrosion potential for carbon steel suggests that this alloy corrodes in a more active mode than the other alloys in both the ambient and elevated temperature environments. This observation is in keeping with previous work on the behavior of metals and alloys in high temperature aqueous systems.[6-8,11-13] The gradual shift in E_{corr} to more noble values with time at elevated temperature is consistent with the formation of a surface film that progressively inhibits the anodic partial reaction. Accordingly, the corrosion potential is expected to shift towards the equilibrium potential for the cathodic partial reaction (hydrogen evolution) as observed in Figs. 1 and 2.

Cyclic Voltammetry

Typical cyclic voltammograms for the ten alloys studied in this work at a temperature of 250°C and after exposure for at least 115 hours are shown in Figs. 3 to 12. For clarity, only the first and third cycles are shown. All voltammograms were recorded by initially sweeping the potential in the noble to active direction from E_{corr}, followed by reversal of the sweep once the potential had been displaced well into the hydrogen evolution region. The active to noble sweep was continued until oxygen evolution occurred, or until the current exceeded 300-400 mA. The sweep was then reversed to complete the cycle.

Of principal interest in this work was the appearance of oxidation and reduction peaks when the potential was cycled between the selected upper and lower limits. The observed current can be expressed in general form as[5]

$$i = C(E)_{dl} \cdot \left(\frac{dE}{dt}\right) + i_F \qquad (1)$$

where $C(E)_{dl}$ is the potential-dependent double-layer capacitance, and i_F is the current due to faradaic (including pseudocapacitive) processes. Peaks in cyclic voltammograms do not necessarily reflect active-to-passive transitions, as is commonly assumed, but may also arise from any charge-transfer process that experiences acceleration, followed by inhibition, as the potential of the metal is varied linearly with time. Examples of such processes include reversible and irreversible reactions involving

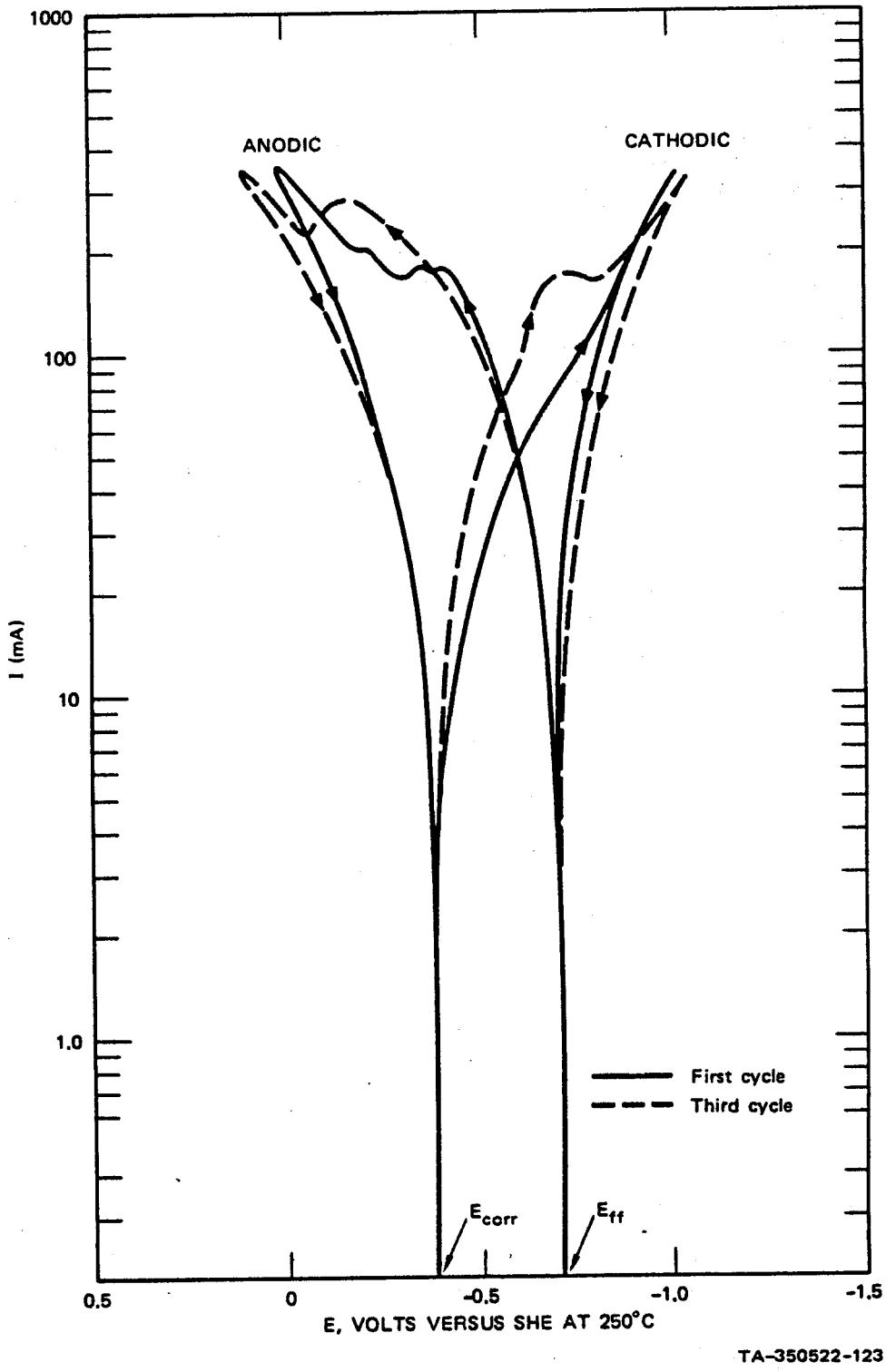

FIGURE 3 CYCLIC VOLTAMMOGRAM FOR AISI TYPE 1010 CARBON STEEL IN HIGH-SALINITY BRINE AT 250°C AFTER 117.5 HOURS EXPOSURE

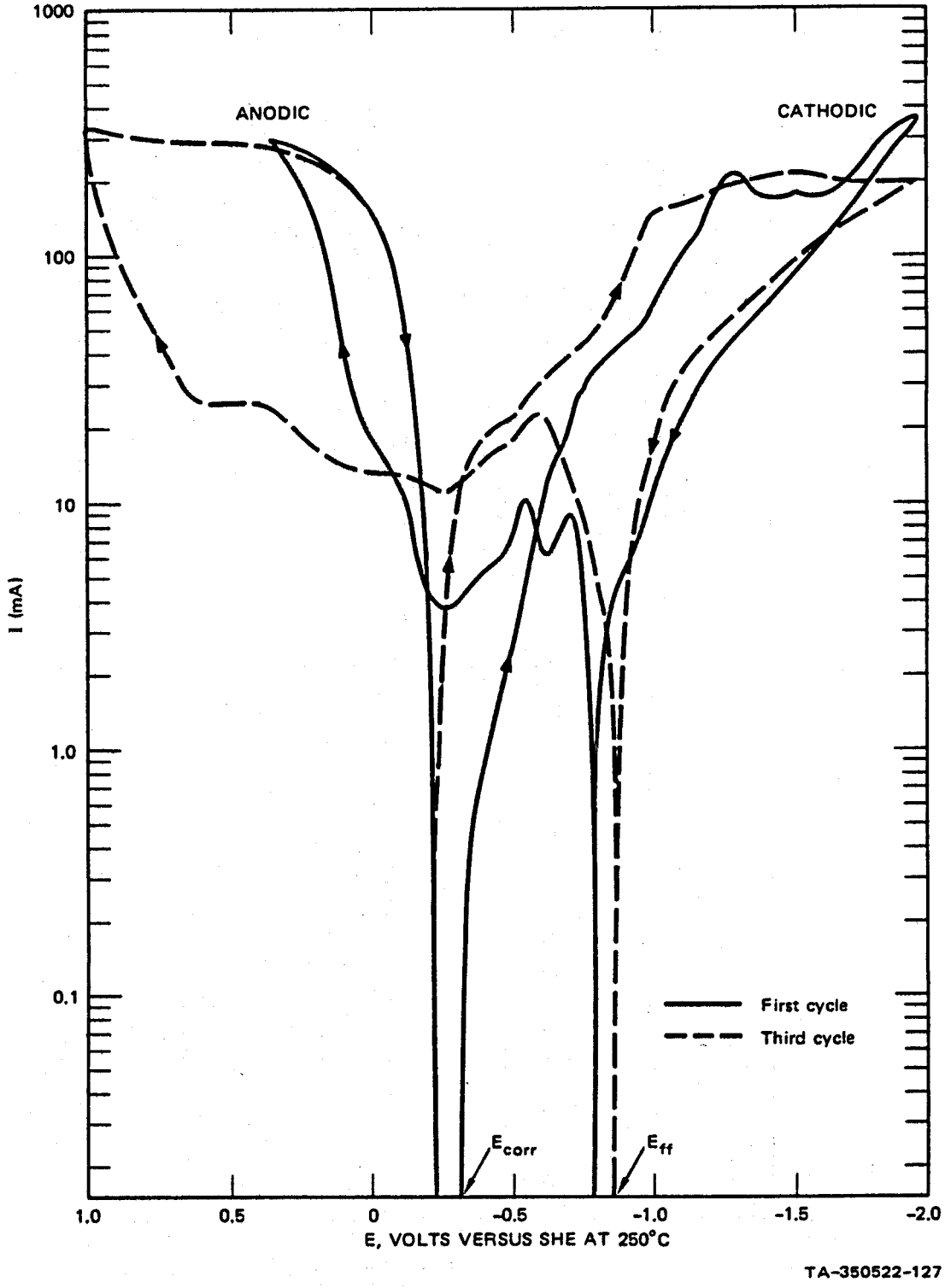

FIGURE 4 CYCLIC VOLTAMMOGRAM FOR E-BRITE 26-1 SS IN HIGH-SALINITY BRINE AT 250°C AFTER 145 HOURS EXPOSURE

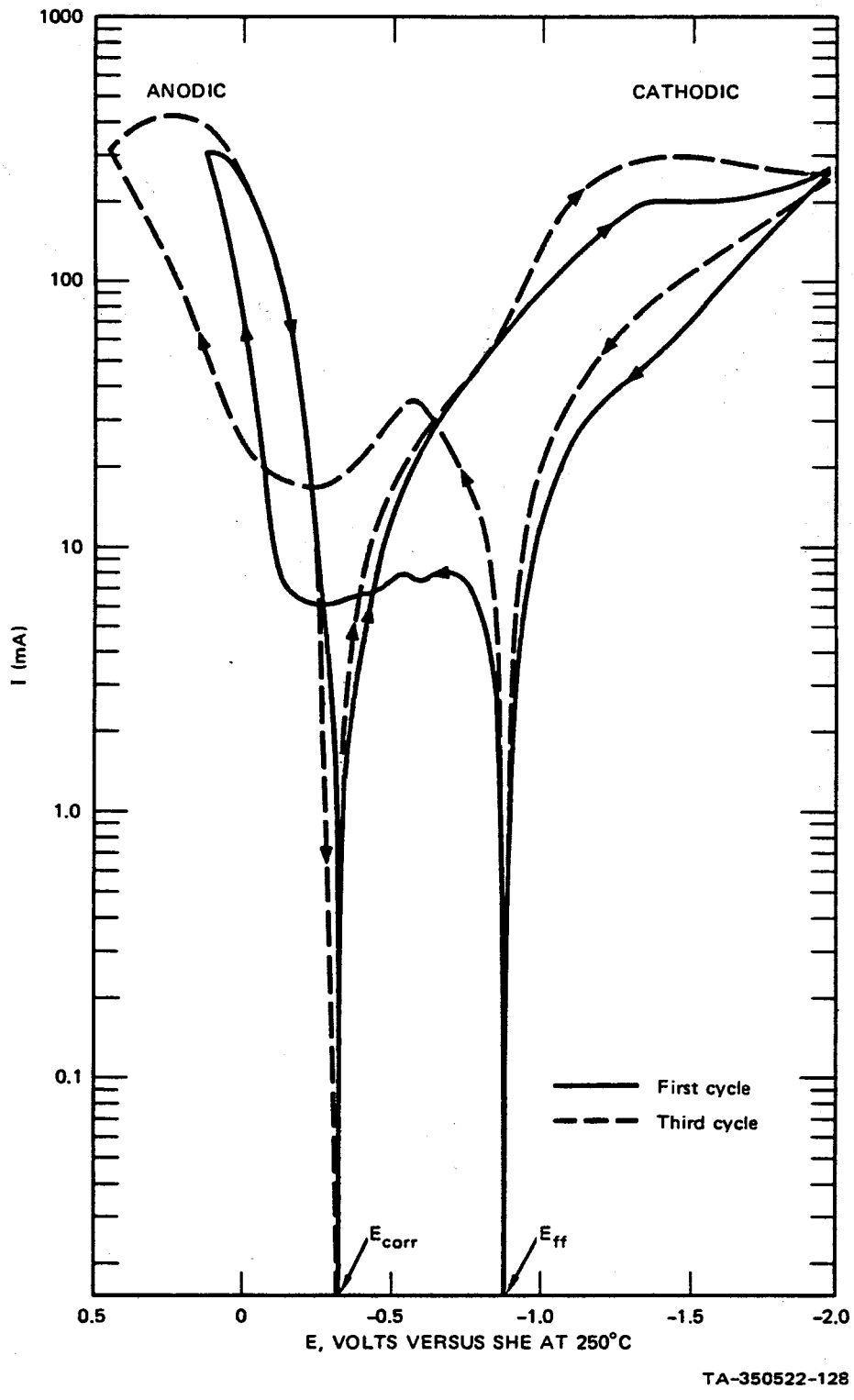

FIGURE 5 CYCLIC VOLTAMMOGRAM FOR 316L SS IN HIGH-SALINITY BRINE AT 250°C AFTER 143.5 HOURS EXPOSURE

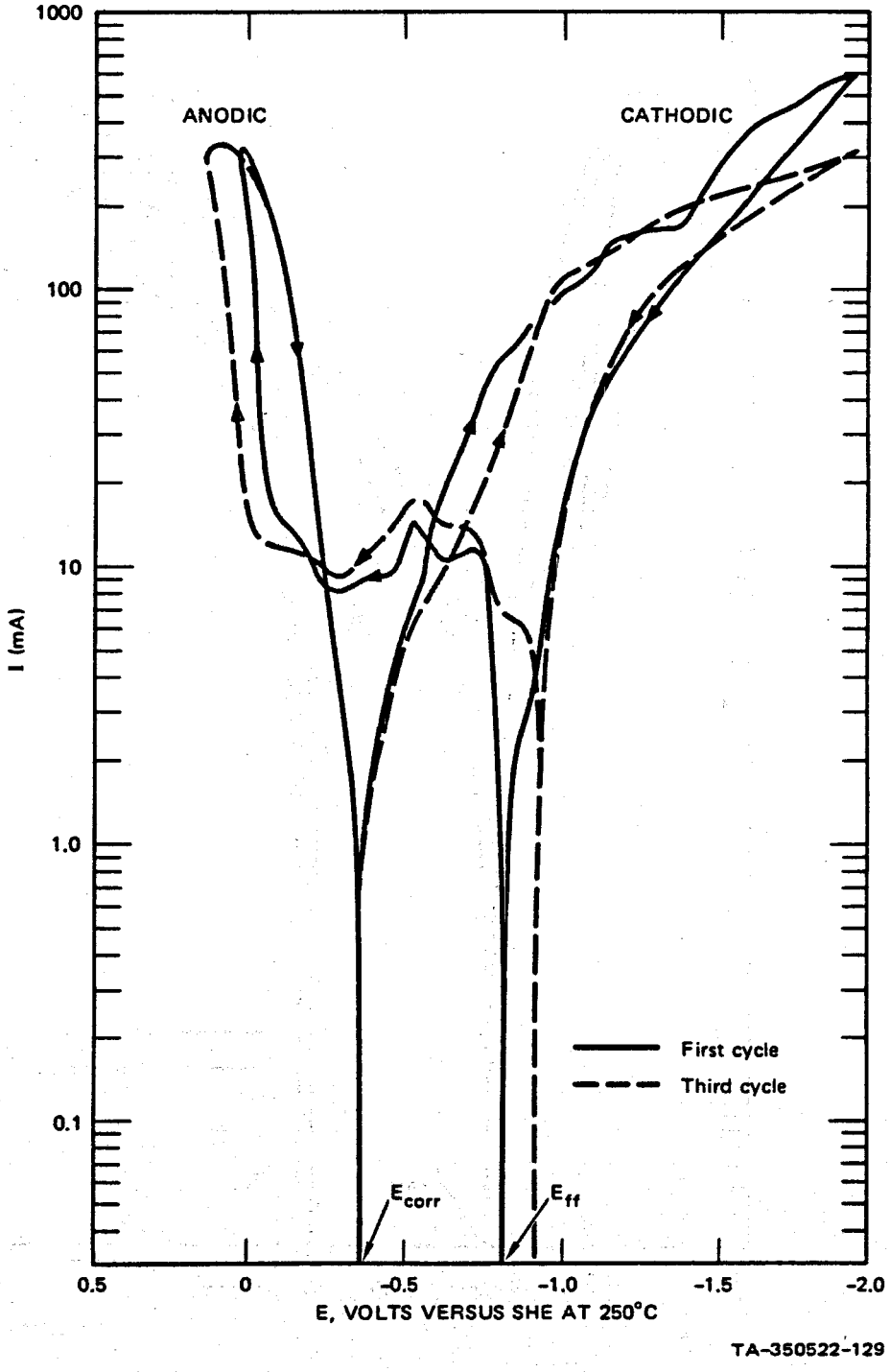

FIGURE 6 CYCLIC VOLTAMMOGRAM FOR HAYNES ALLOY 20 MOD. IN HIGH-SALINITY BRINE AT 250°C AFTER 143 HOURS EXPOSURE

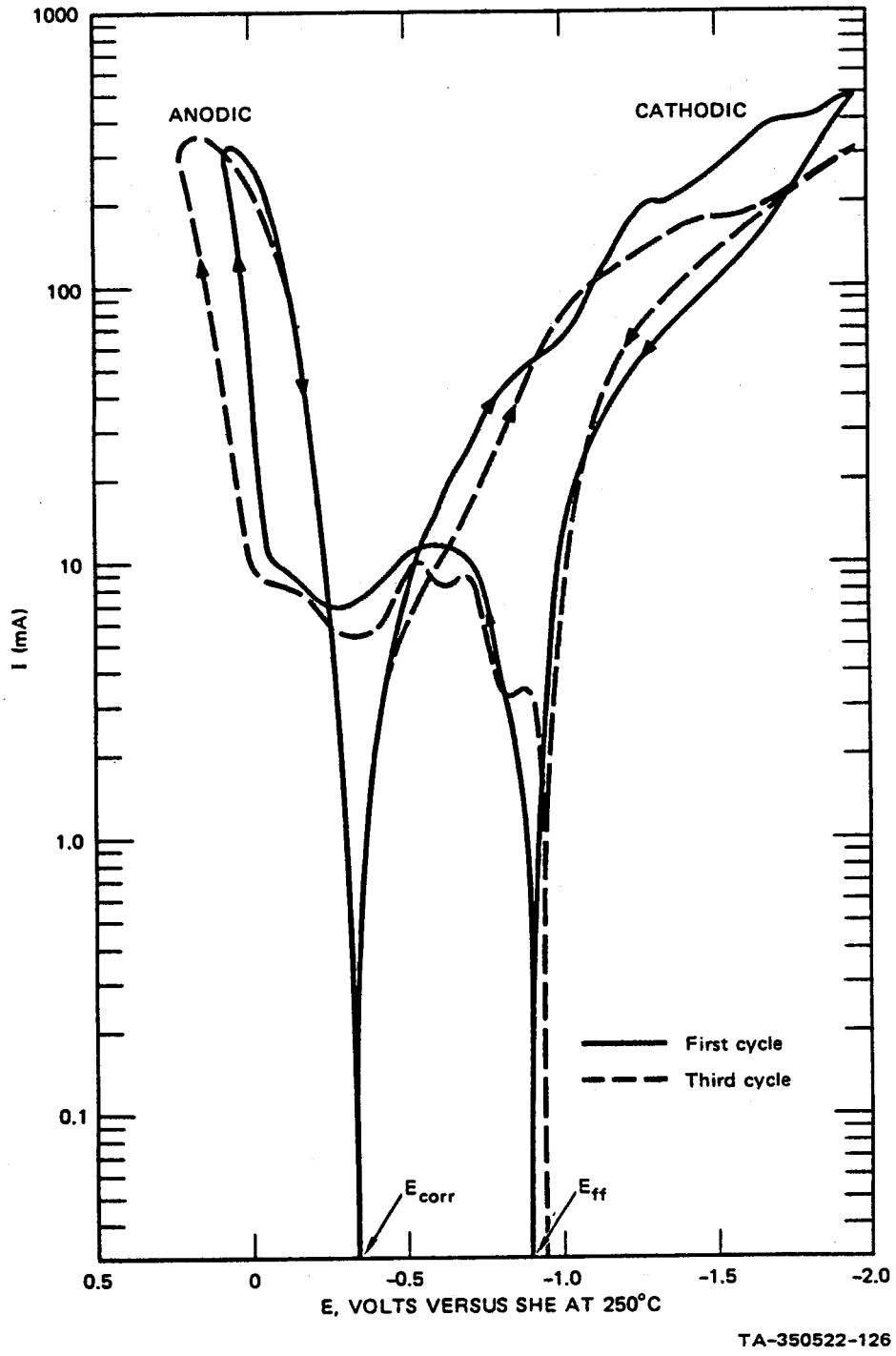

FIGURE 7 CYCLIC VOLTAMMOGRAM FOR CARPENTER 20Cb-3 IN HIGH-SALINITY BRINE AT 250°C AFTER 144 HOURS EXPOSURE

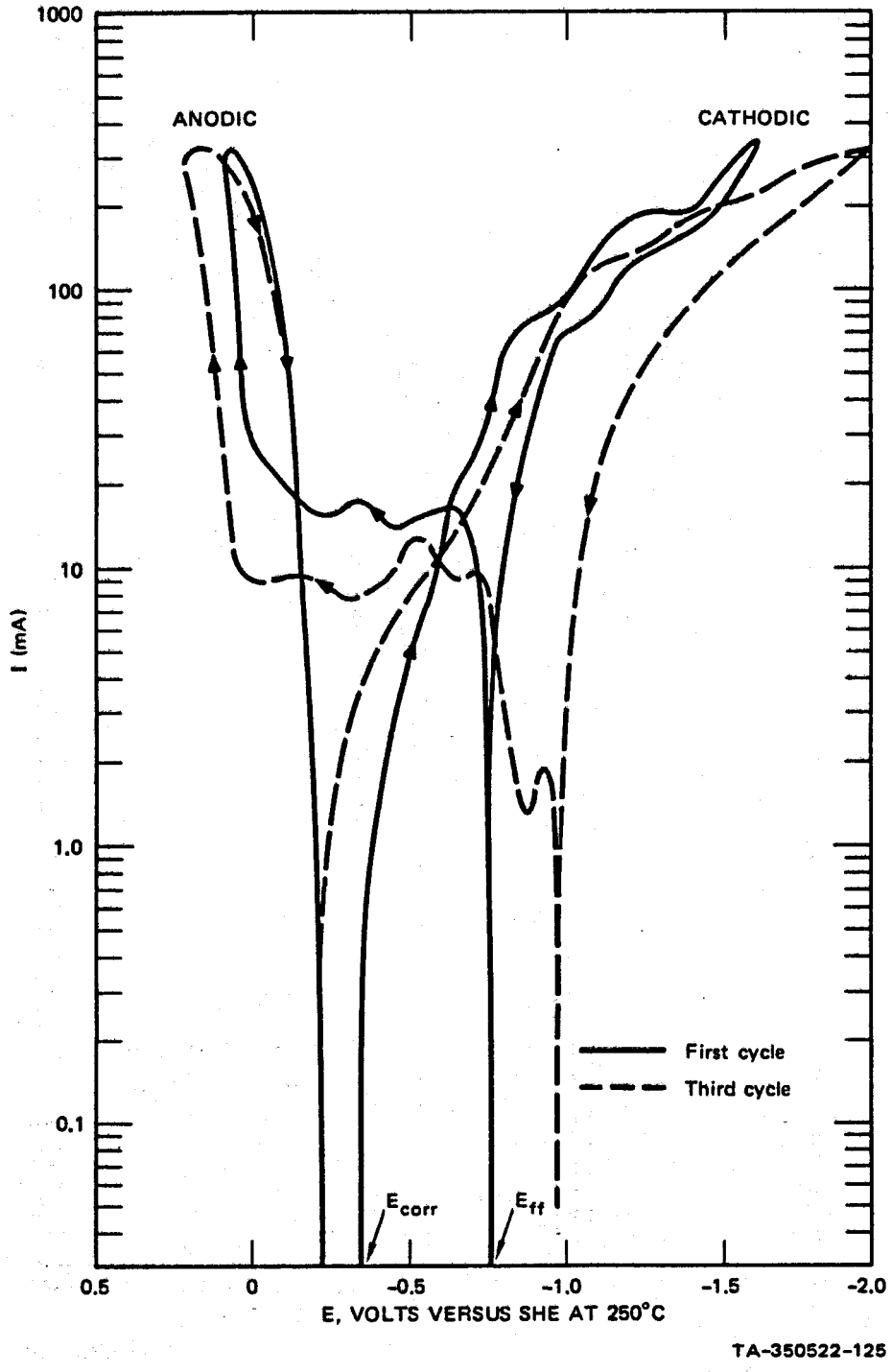

FIGURE 8 CYCLIC VOLTAMMOGRAM FOR INCONEL ALLOY 625 IN HIGH-SALINITY BRINE AT 250°C AFTER 118.5 HOURS EXPOSURE

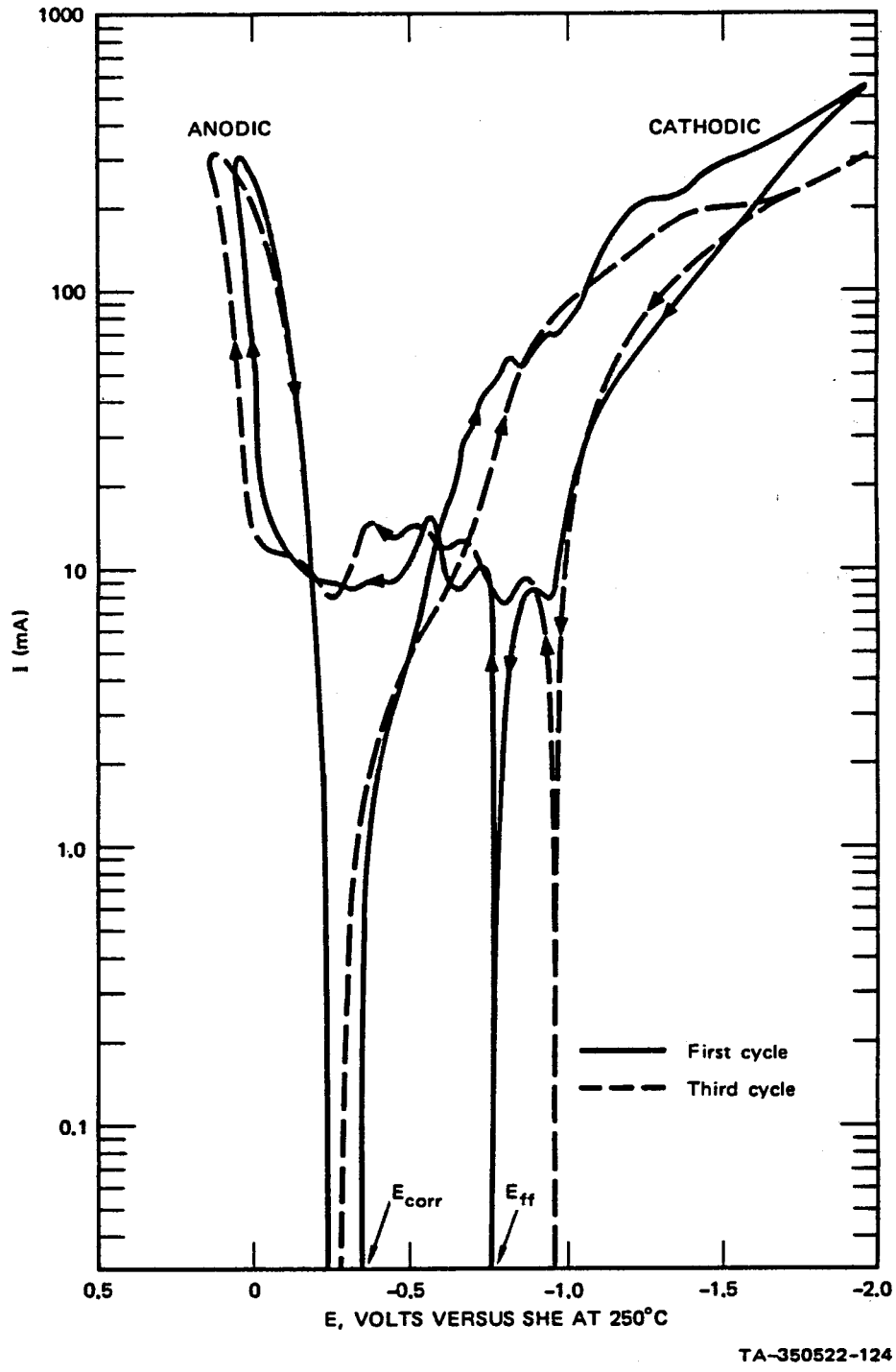

FIGURE 9 CYCLIC VOLTAMMOGRAM FOR HASTELLOY ALLOY G IN HIGH-SALINITY BRINE AT 250°C AFTER 145.5 HOURS EXPOSURE

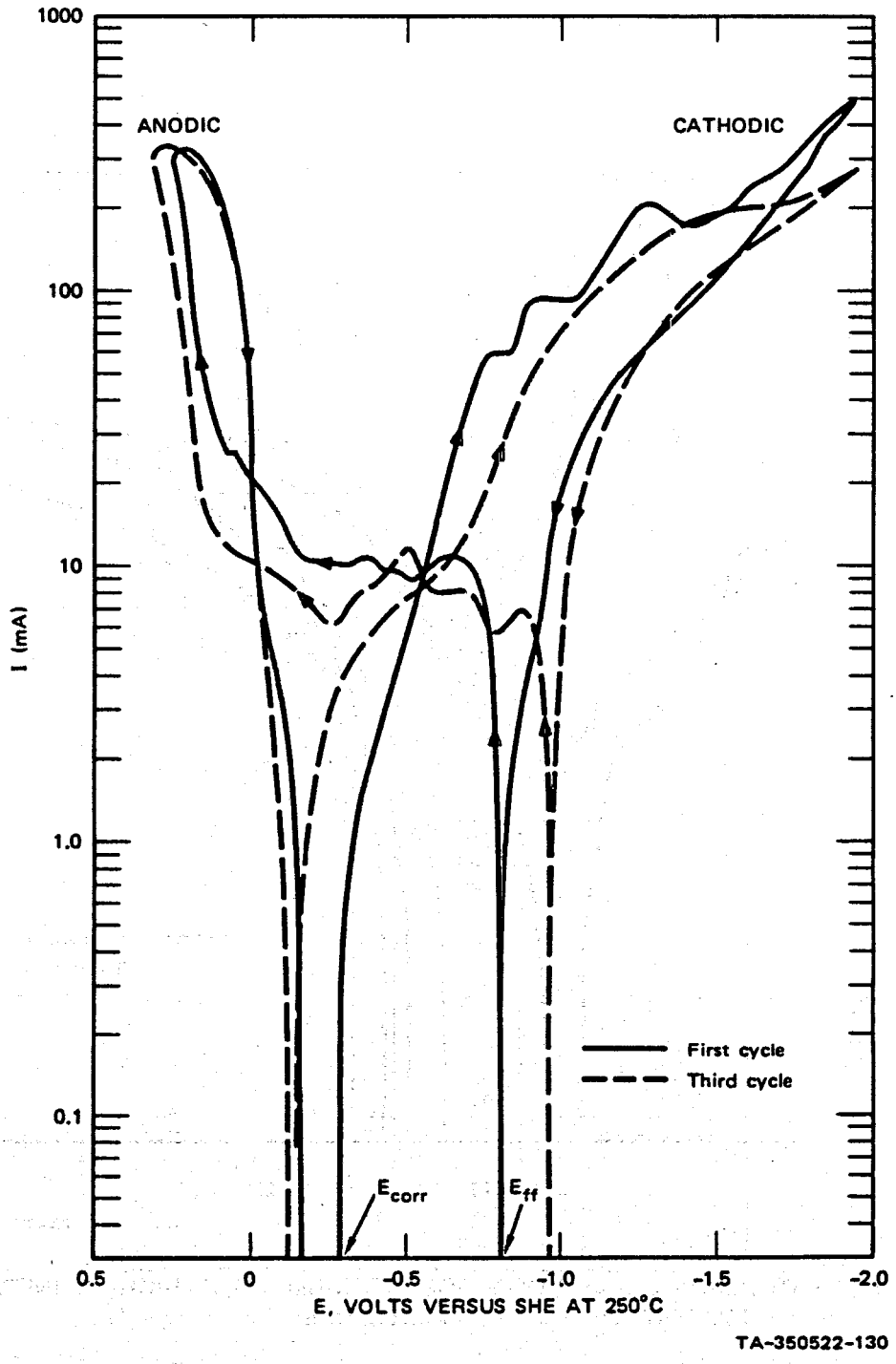

FIGURE 10 CYCLIC VOLTAMMOGRAM FOR HASTELLOY ALLOY C-276 IN HIGH-SALINITY BRINE AT 250°C AFTER 144.5 HOURS EXPOSURE

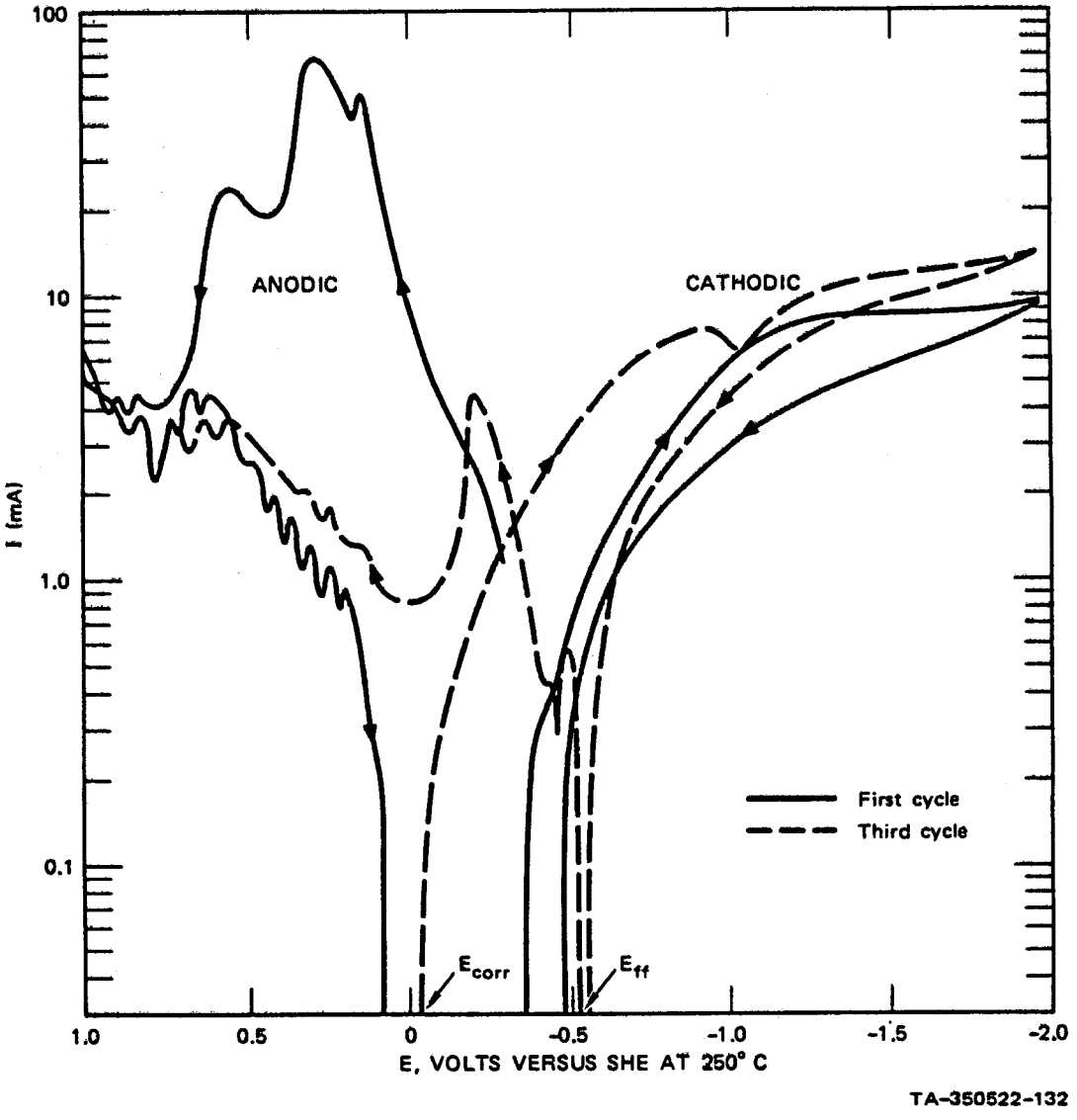

FIGURE 11 CYCLIC VOLTAMMOGRAM FOR TITANIUM 50A IN HIGH-SALINITY BRINE AT 250°C AFTER 120 HOURS EXPOSURE

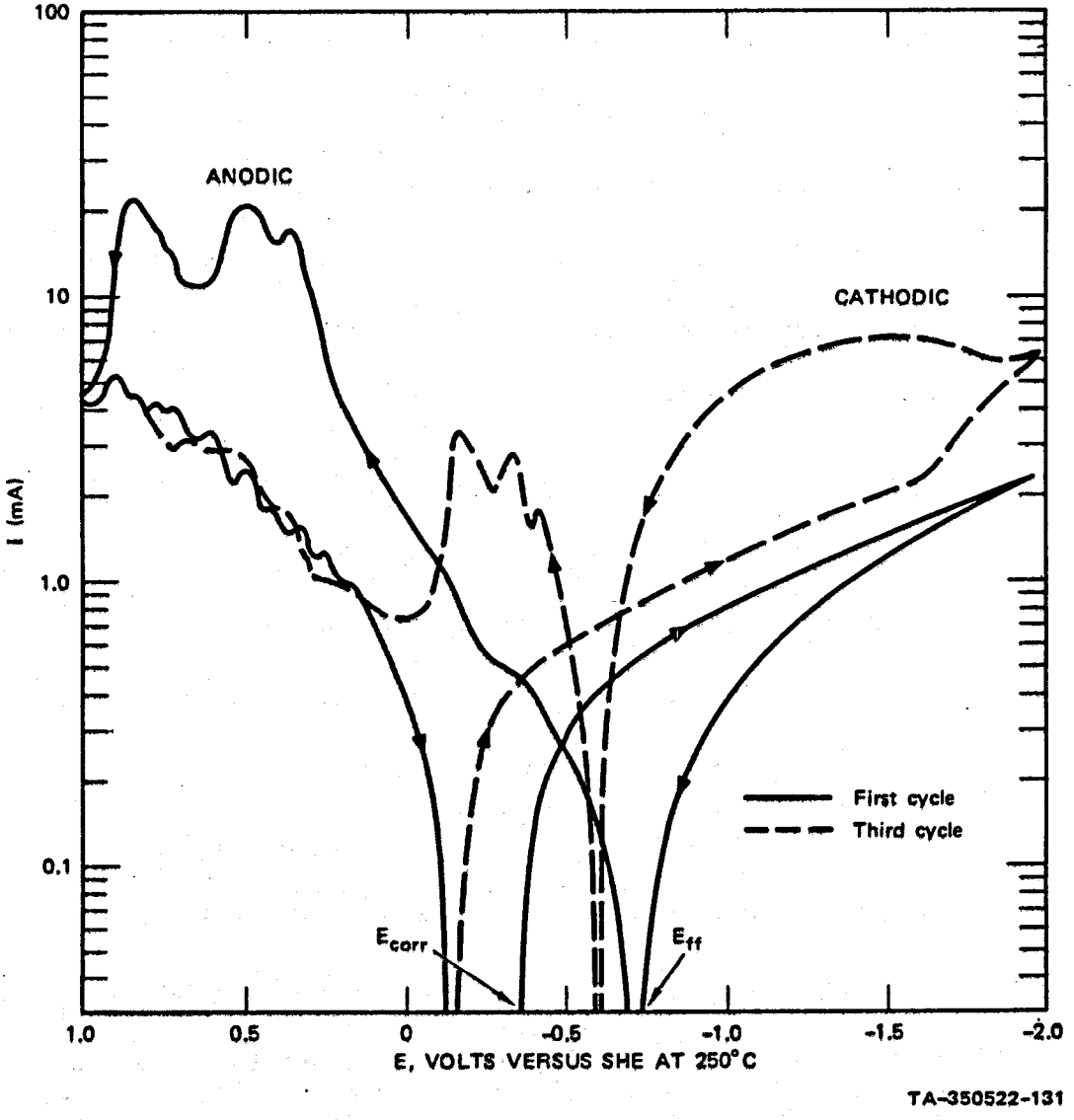

FIGURE 12 CYCLIC VOLTAMMOGRAM FOR TiCODE 12 IN HIGH-SALINITY BRINE AT 250°C AFTER 146 HOURS EXPOSURE

diffusion of dissolved reactants and products, and the formation of surface films via electrochemical adsorption of oxide or other ions onto the alloy surface,[5] in addition to the commonly assumed active-to-passive transitions. In principal, it is possible to differentiate between these various processes by analyzing the peak potential and current as a function of sweep-rate.[5,14] However, few of the transition metals and their alloys exhibit sufficiently reproducible voltammograms to make this type of analysis possible. This problem is well illustrated in the present work by a comparison of the first and third cycles for each alloy. Thus, for most of the materials studied, multiple cycling not only seriously affects the peak currents and potentials, but also leads to a change in the number of peaks observed. In view of the complex nature of cyclic voltammetric response, no attempt was made in this work to determine the sweep-rate dependencies of the peak currents and peak potentials. Instead, equivalent peaks in the three potential cycles were compared, and the most active oxidation peak potentials and the most noble reduction peak potentials were used for comparison with calculated equilibrium potentials for selected reactions involving pure components of the alloys.

For most of the materials studied (with the possible exception of the titanium alloys), the initial sweep of the potential in the noble-to-active direction from E_{corr} probably reduced the surface films. Accordingly, the potential (E_{ff}) at which the current changes from cathodic to anodic on the subsequent active-to-noble sweep defines a

pseudo-corrosion state (i.e., $i_a + i_c = 0$, where i_a and i_c are the partial anodic and cathodic currents, respectively) in which inhibition of the partial anodic process by a surface film has been eliminated, or at least greatly reduced. Simple argument on the basis of the Wagner-Traud mechanism for electrochemical corrosion shows that E_{ff} should be more active than the true, spontaneous, corrosion potential E_{corr}, as observed in Table 3.

All of the high-nickel and high-chromium alloys studied in this work exhibit a region of inverse hysteresis when the sweep is reversed at high noble potentials, with the current on the noble-to-active sweep exceeding that observed on the active-to-noble sweep. This behavior is characteristic of localized attack, such as pitting, and will be discussed in detail in a following paper.[15]

DISCUSSION

Potential-pH Diagrams For Sulfide-Free Systems

Potential-pH diagrams for iron (Figs. 13 and 14), nickel (Figs. 15 and 16), chromium (Figs. 17 and 18) and titanium (Figs. 19 and 20) in sulfide-free high salinity brine (3.6-m NaCl) at 25°C and 250°C were derived using previously described techniques.[16-20] A detailed discussion of the computational methods employed is given elsewhere,[2-4,20] and a listing of the species considered, together with the thermodynamic parameters used, may be found in Ref. 2. Briefly, equilibrium potentials and solubility relationships for

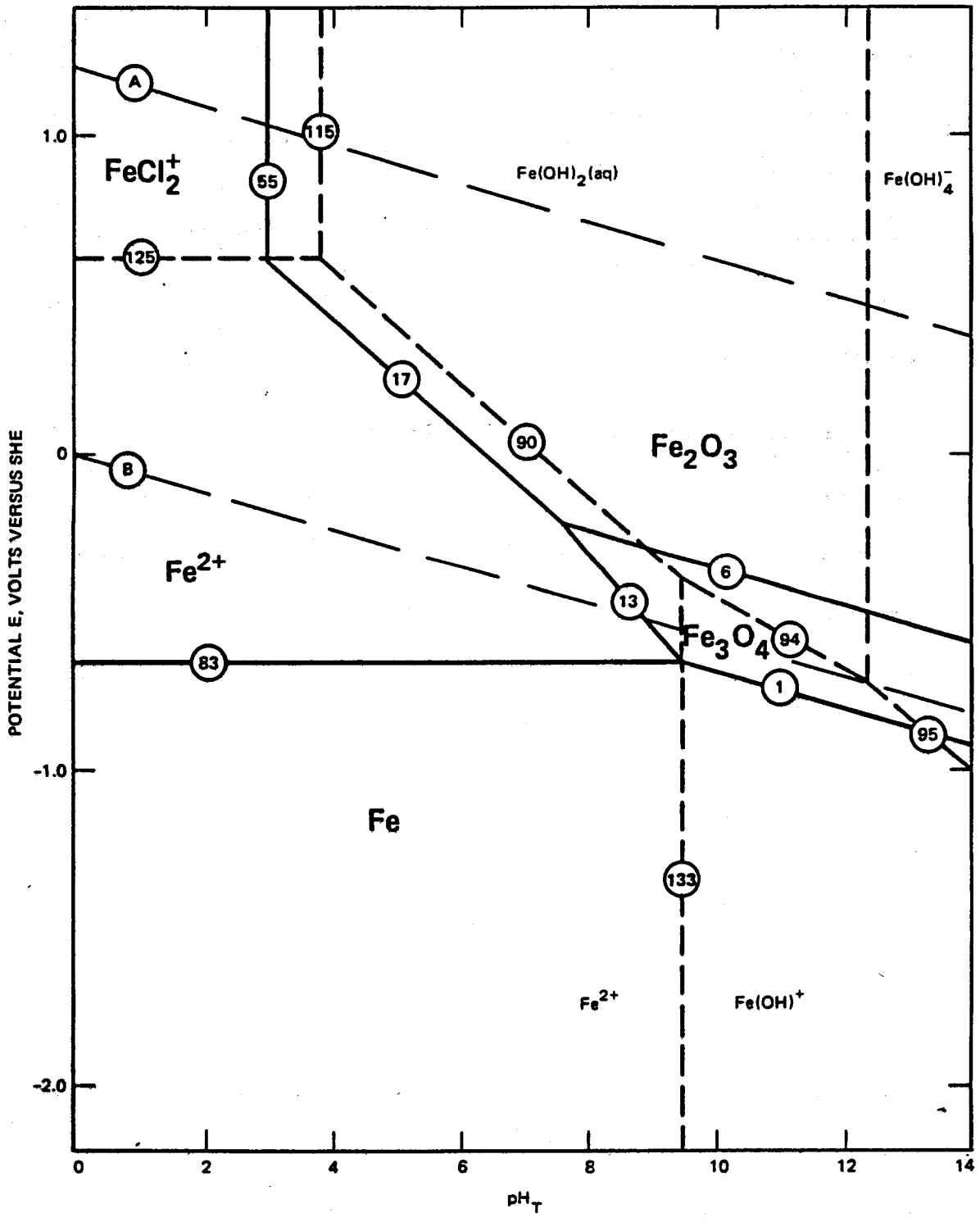

NOTE: (aq) designates soluble molecular species.

SA-5308-33

FIGURE 13 POTENTIAL-pH DIAGRAM FOR IRON IN HIGH-SALINITY BRINE AT 25°C

Activities of dissolved iron species = 10^{-6} molal.

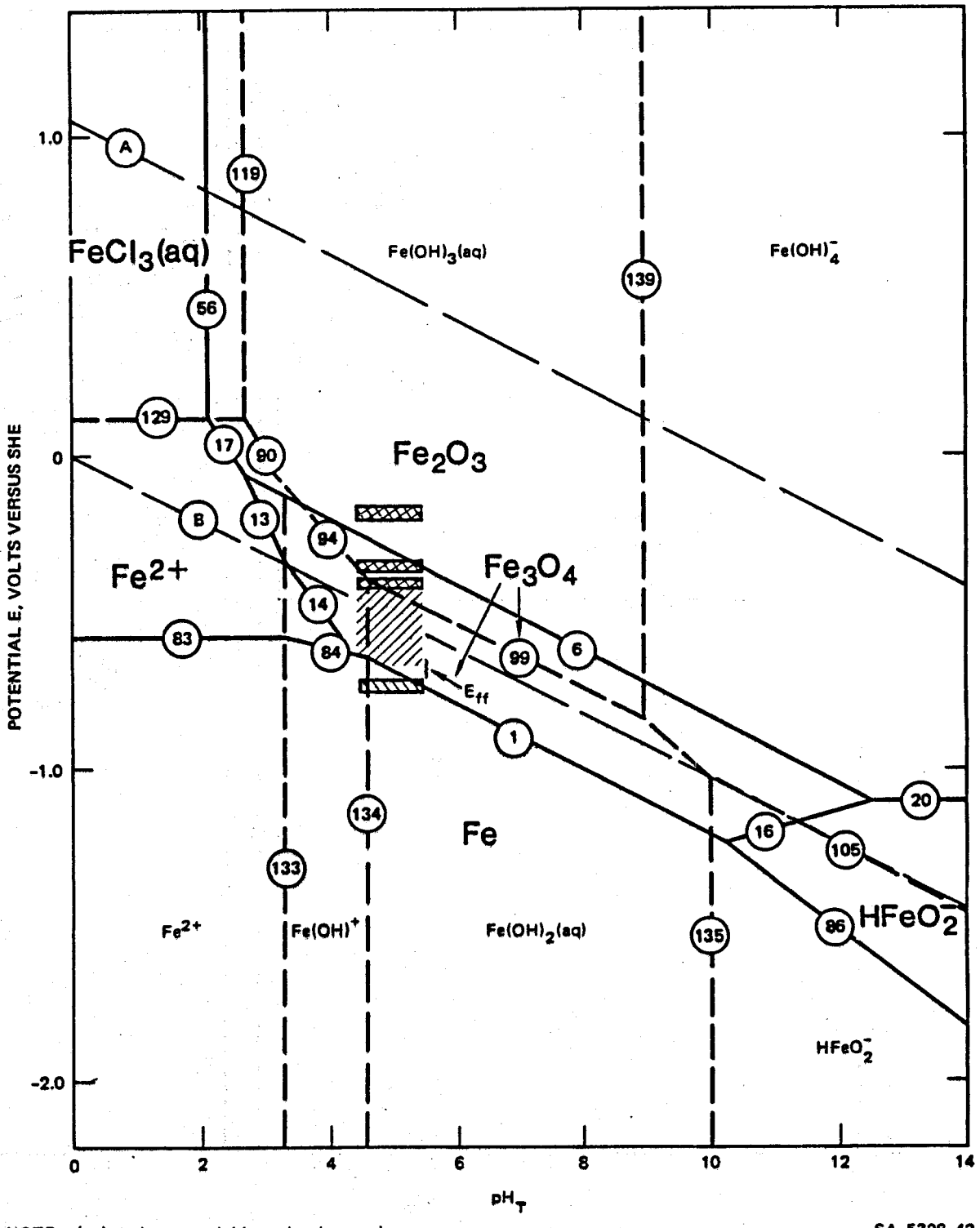

FIGURE 14 POTENTIAL-pH DIAGRAM FOR IRON IN HIGH-SALINITY BRINE AT 250°C

Activities of dissolved iron species = 10^{-4} molal. //// – E_{corr} for carbon steel, ▨ – oxidation peak potential for carbon steel, ▧ – reduction peak potentials for carbon steel (see Table 3).

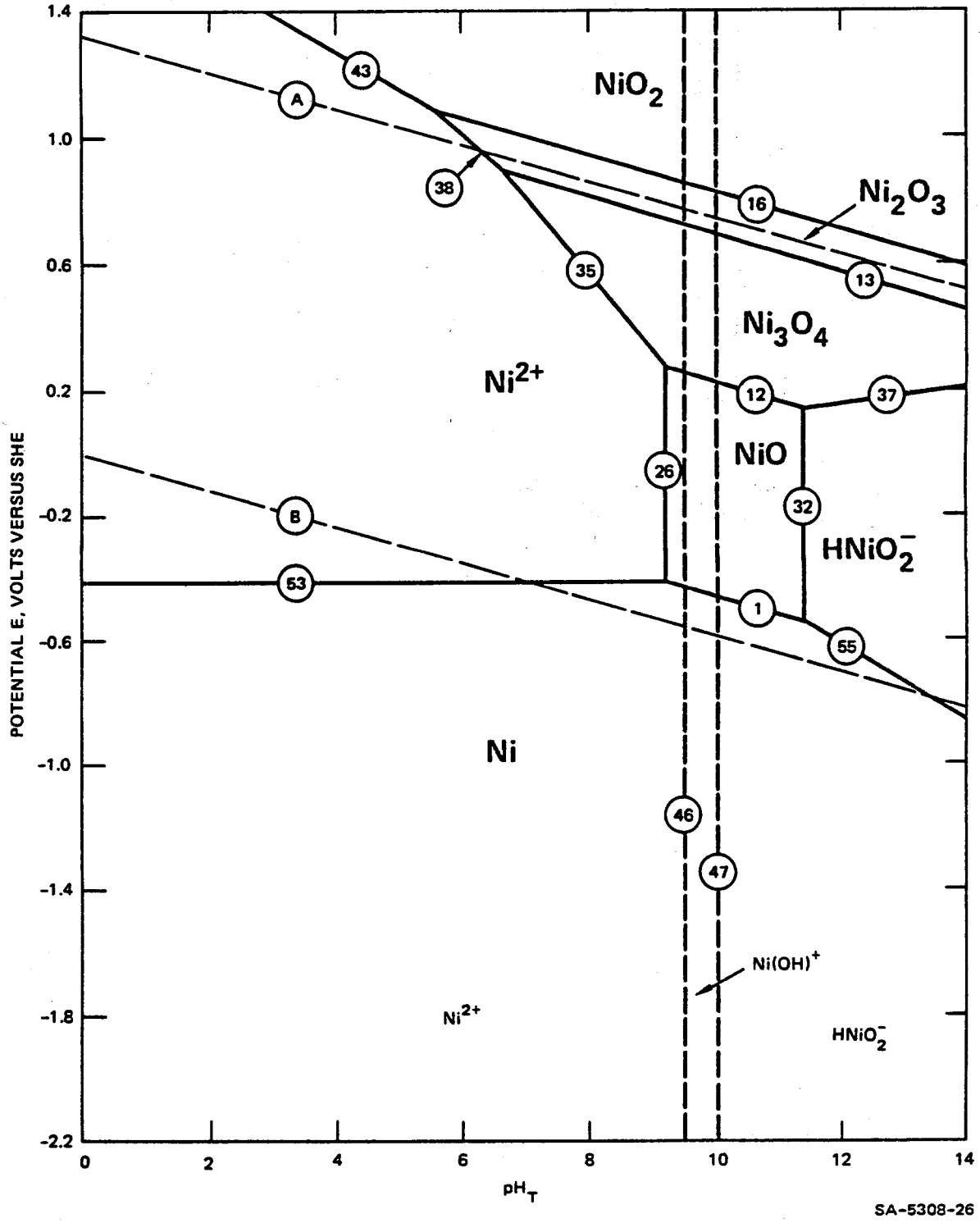

FIGURE 15 POTENTIAL-pH DIAGRAM FOR NICKEL IN HIGH-SALINITY BRINE AT 25°C

Activities of dissolved nickel species = 10^{-6} molal.

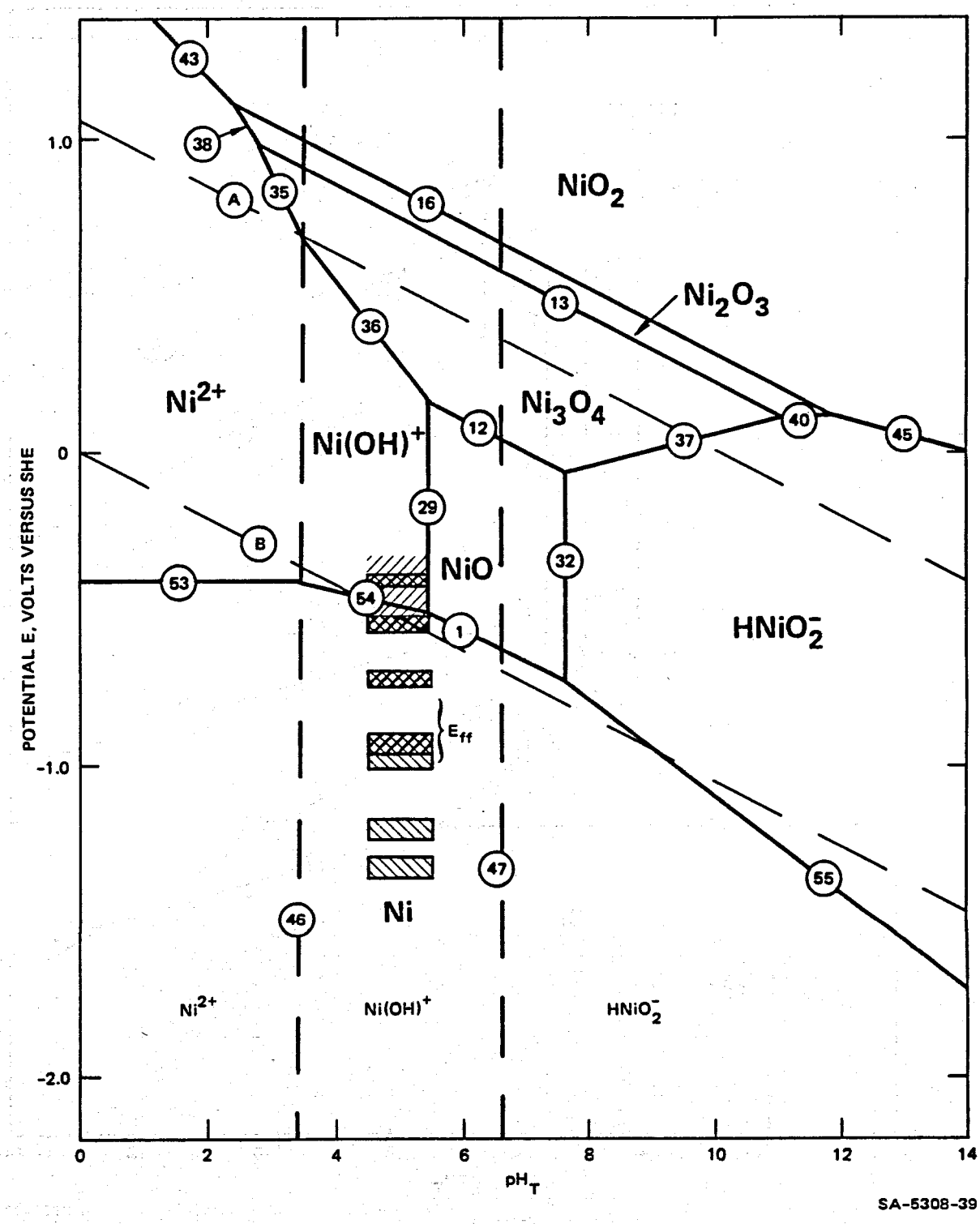

FIGURE 16 POTENTIAL-pH DIAGRAM FOR NICKEL IN HIGH-SALINITY BRINE AT 250°C

Activities of dissolved nickel species = 10^{-6} molal. //// – E_{corr} for nickel-based alloys, ▨ – oxidation peak potentials for nickel-based alloys, ▨ – reduction peak potentials for nickel-based alloys (see Table 3).

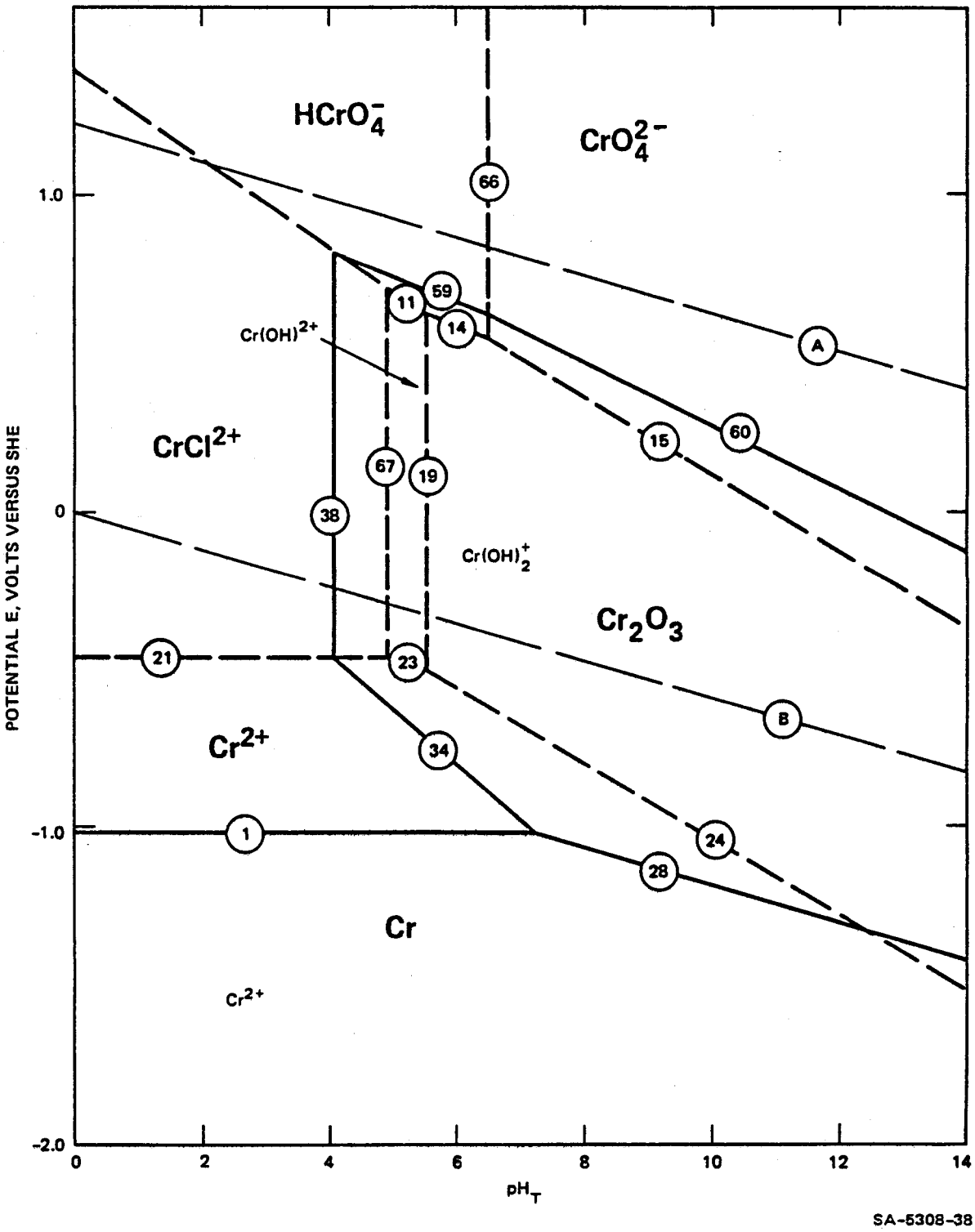

FIGURE 17 POTENTIAL-pH DIAGRAM FOR CHROMIUM IN HIGH-SALINITY BRINE AT 25°C

Activities of dissolved chromium species = 10^{-6} molal.

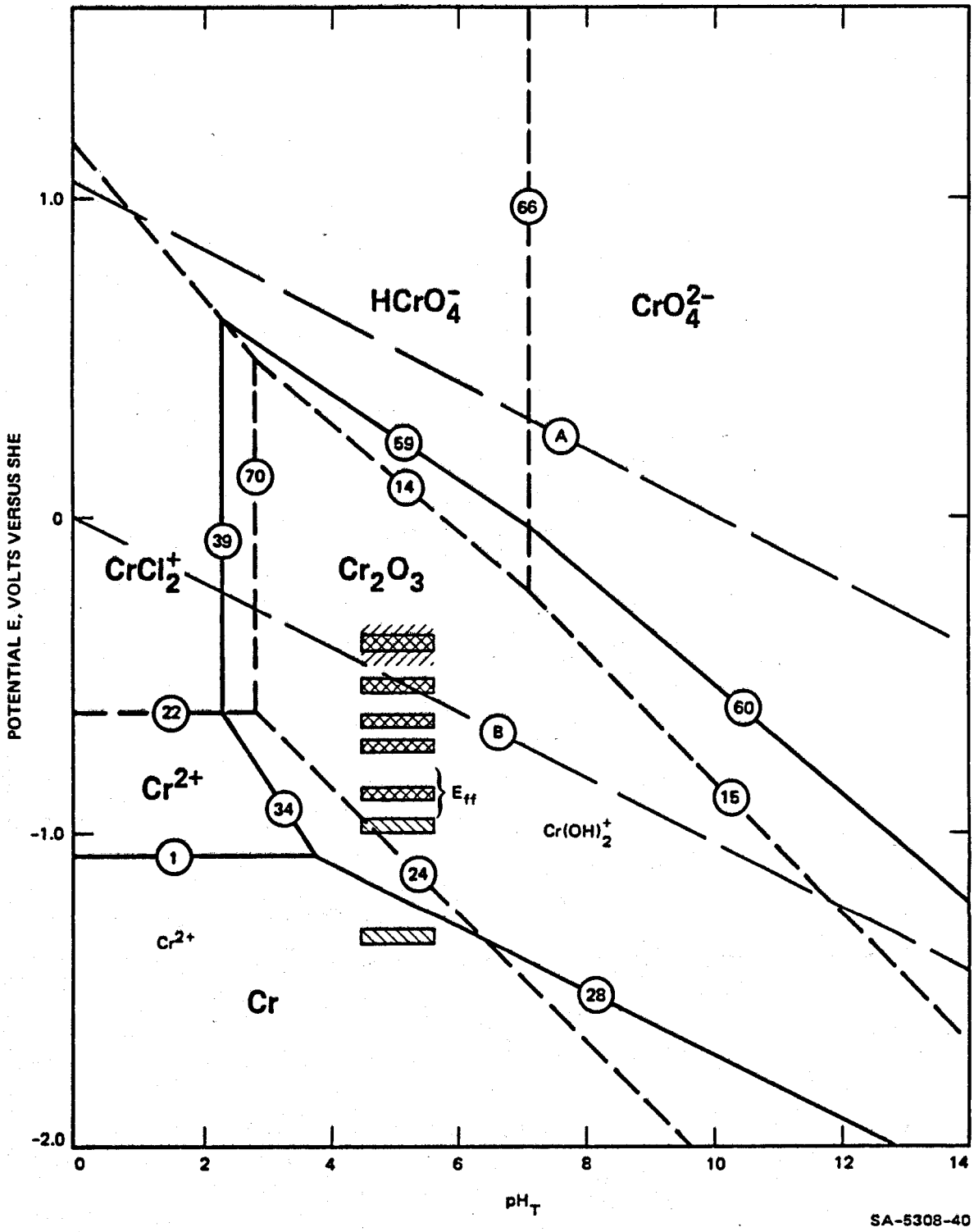

FIGURE 18 POTENTIAL-pH DIAGRAM FOR CHROMIUM IN HIGH-SALINITY BRINE AT 250°C

Activities of dissolved chronium species = 10^{-6} molal. //// – E_{corr} for high chromium alloys (>15 wt%), ▨ – oxidation peak potential for high chromium alloy, ▨ – reduction peak potential for high chromium alloy.

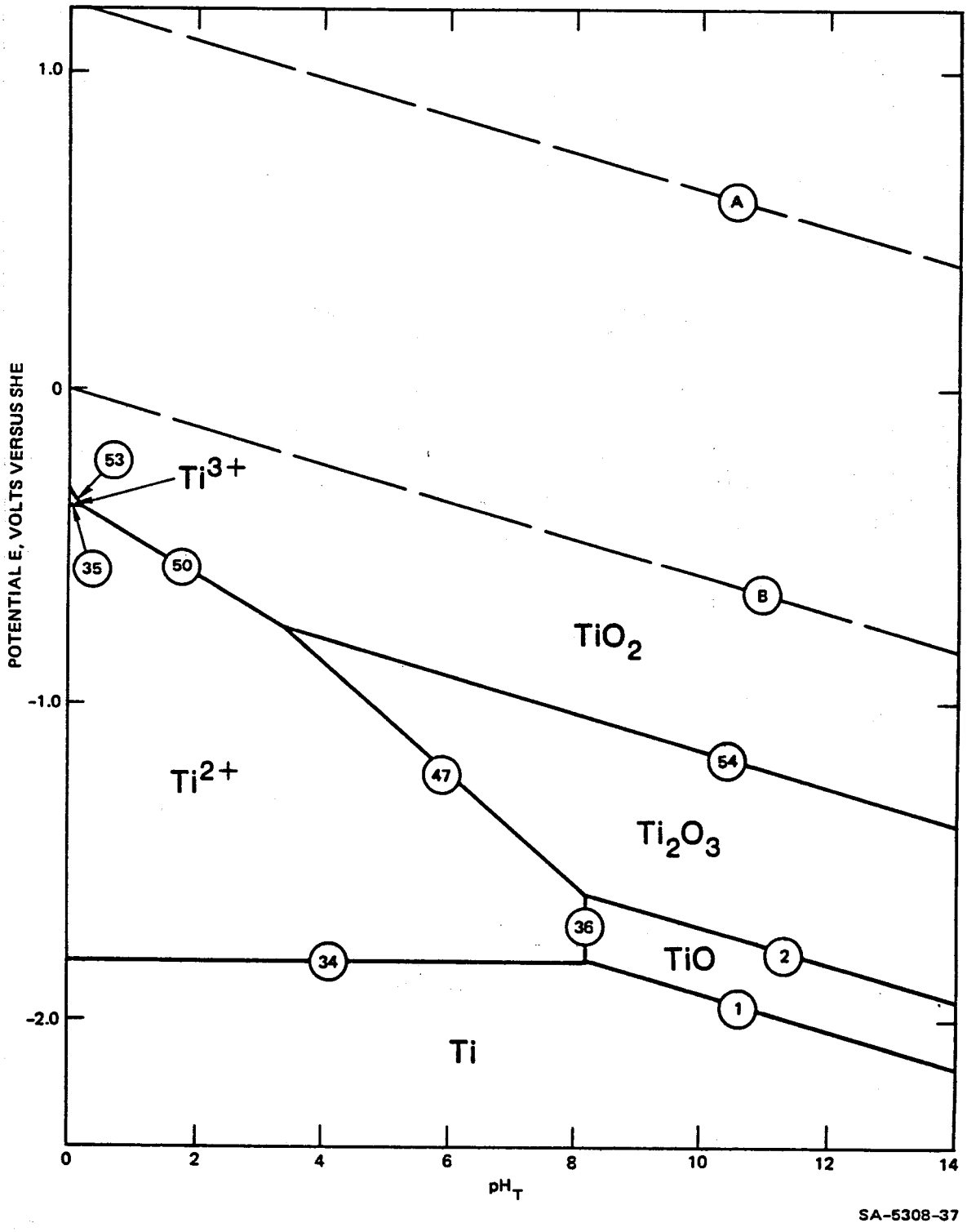

FIGURE 19 POTENTIAL-pH DIAGRAM FOR TITANIUM IN HIGH-SALINITY BRINE AT 25°C

Activities of dissolved titanium species = 10^{-6} molal.

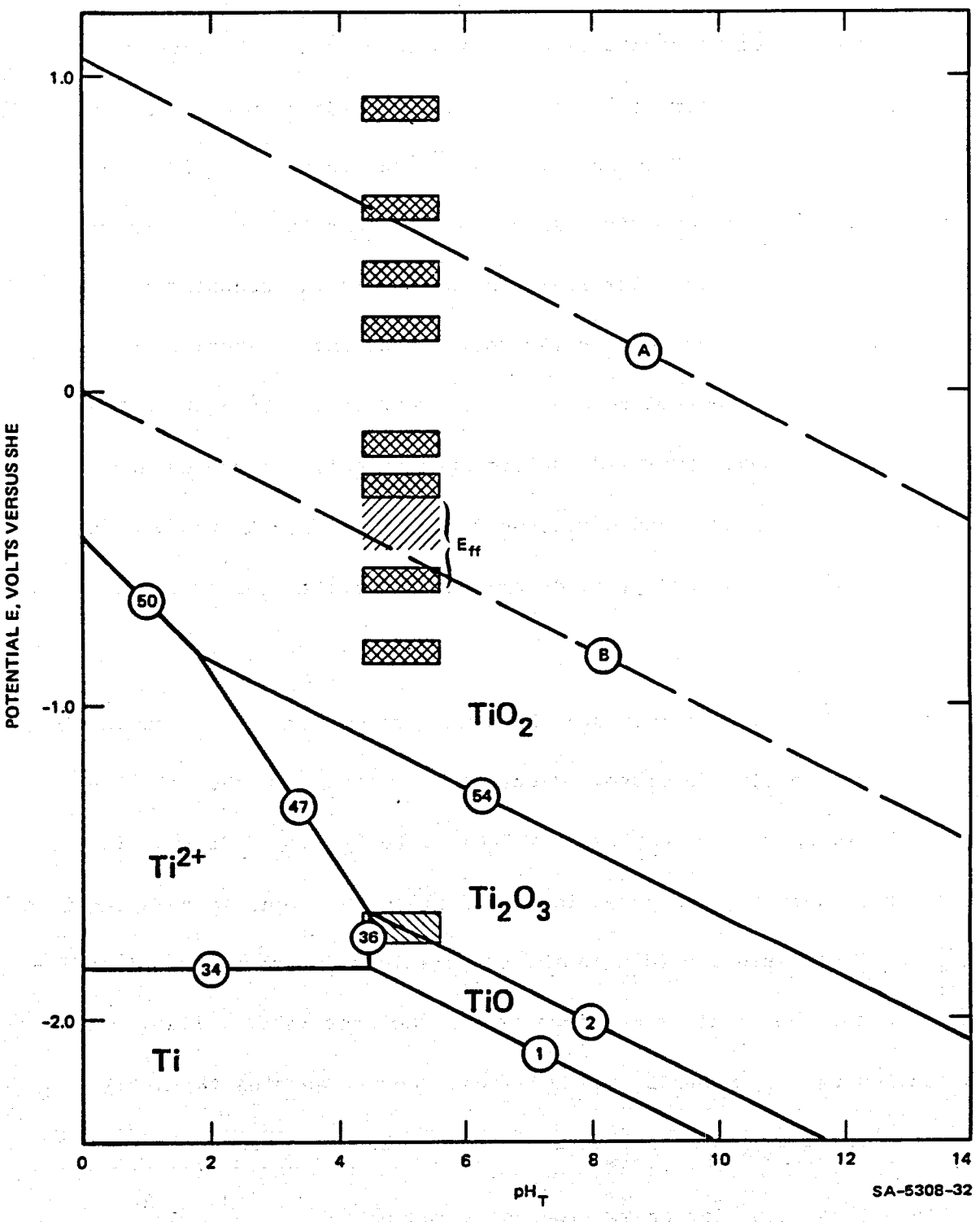

FIGURE 20 POTENTIAL-pH DIAGRAM FOR TITANIUM IN HIGH-SALINITY BRINE AT 250°C

Activities of dissolved titanium species = 10^{-6} molal. //// – E_{corr} for titanium-based alloys, ▩ – oxidation peak potential for titanium-based alloys, ▨ – reduction peak potentials for titanium-based alloys.

reactions at elevated temperatures were calculated using the linear heat capacity approximation for dissolved components as developed by Naumov et al.[21] and subsequently used by Macdonald and Hyne[20] and later by Taylor.[22] The thermodynamic data were taken from a single compilation,[21] whenever possible, so as to maintain internal consistency in the computations. Equilibrium relationships between two solid components or between a solid component and a dissolved species are represented by solid lines, whereas reactions that involve dissolved species only are represented by broken lines. Lines A and B represent the limits for thermodynamic stability of water, and are plotted for unit fugacities for hydrogen and oxygen.

Only in the cases of iron and chromium were sufficient thermodynamic data available to include dissolved chloride complexes in the calculations. Accordingly, the complex ions $FeCl^{2+}$, $FeCl_2^+$, and $FeCl_3(aq)$ were considered in deriving the potential-pH diagrams for iron, whereas the ions $CrCl^{2+}$ and $CrCl_2^+$ were included in the computations for chromium. Insufficient data for the divalent metal-chloride complexes were available, so that species of the type MCl^+ and $MCl_2(aq)$, where M denotes the metal under consideration, could not be included in the derivations.

Since ions with high charge-to-radius ratios (e.g., Fe^{3+}, Cr^{3+}, Ti^{4+}) tend to hydrolyze at elevated temperatures,[23,24] we attempted to include hydrolyzed ions in the calculations. Thus, hydrolyzed species such as $Ni(OH)^+$, $HNiO_2^-$, TiO_2^{2+}, $Cr(OH)_2^+$, $Cr(OH)_2^+$, $H_2CrO_4(aq)$,

$HCrO_4^-$, CrO_4^{2-}, $Fe(OH)^+$, $Fe(OH)_2(aq)$, $HFeO_2^-$, $Fe(OH)^{2+}$, $Fe(OH)_2^+$, $Fe(OH)_3(aq)$ and $Fe(OH)_4^-$ have been considered. Only those ions that exhibit fields of predominance appear in the potential-pH diagrams. However, a complete listing of the equilibrium properties of reactions that involve all of the species listed above is given in Reference 2.

Only metal oxide and oxyhydroxides (e.g., FeOOH) solid phases were considered in this work for three reasons. First, only sparse heat capacity data are available for metal hydroxides such as $Ni(OH)_2$ and $Ni(OH)_3$. Second, the crystallographic states of the hydroxides for which data are available are frequently ill-defined, so that it is not always possible to decide if the phase considered is the most stable. Finally, many of the hydroxides are thermodynamically unstable with respect to the oxides at evelated temperatures, so that only the latter should be considered in the derivations. It should be noted, however, that the hydroxides are frequently stable with respect to the oxides at ambient temperature, and their omission from the diagrams reported here for 25°C is due to lack of data.

The effect of temperature on the thermodynamic behavior of each metal in sulfide-free brine may be ascertained by comparing the diagrams at 25°C and 250°C. Thus, in the cases of iron (Figs. 13 and 14) and chromium (Figs. 17 and 18), a principal effect of temperature in the acid region is to change the identity of the predominant dissolved species under oxidizing conditions from $FeCl_2^+$ and $CrCl^{2+}$ at 25°C to $FeCl_3(aq)$ and $CrCl_2^+$ at 250°C.

This change is expected, because it is known that the dielectric constant for water decreases as the temperature is increased. Thus, the higher complexes with lower charge-to-radius ratios become more stable due to the more favorable electrostatic energy of the ion in the aqueous medium at elevated temperatures.

An increase in temperature also decreases the stability regions for dissolved cationic species at low pH, but leads to an increase in the stability regions for anionic species at high pH. In the latter case, the increased stability of ions of the type HMO_2^- is due to a shift in the equilibrium line for the HMO_2^-/M couple to lower potentials, as well as a shift in the oxide dissolution reactions (e.g., $NiO \rightarrow HNiO_2^-$) to lower pH values. These predicted relationships indicate that both iron and nickel may be more susceptible to corrosion in alkaline systems at elevated temperatures. Experimental data[6,11] support this contention. The calculated behavior of chromium at 25°C (Fig. 17) and 250°C (Fig. 18) shows that the equilibrium lines for the oxidative dissolution of chromic oxide (Cr_2O_3) to form the Cr(VI) species $HCrO_4^-$ and CrO_4^{2-} shift to more negative potentials as the temperature is increased. The consequences of this shift for the pitting tendencies of alloys containing chromium in high-salinity geothermal brines at elevated temperatures are discussed elsewhere.[15]

Thermodynamic Analyses of the Corrosion and Cyclic Voltammetric Peak Potentials

In analyzing the corrosion potential behavior and the cyclic voltammograms for the various alloys in terms of the predicted thermodynamic behavior of the component metals, it is necessary first to establish expected relationships between the observed cyclic voltammetric peak potentials, the corrosion potentials, and the equilibrium potentials plotted in the diagrams. Theoretical arguments[6,11] dictate that since the overpotentials for anodic (oxidation) and cathodic (reduction) processes are positive and negative, respectively, the following inequalities should be obeyed:

$$E_p^a > E_{eq} \tag{2}$$

$$E_p^c < E_{eq} \tag{3}$$

where subscripts p and eq denote peak and equilibrium properties, and superscripts a and c denote anodic and cathodic processes. For conjugate oxidation/reduction peaks--that is, for peaks that arise from the same electrochemical process--the inequalities become more restrictive:

$$E_p^c < E_{eq} < E_p^a \tag{4}$$

Similarly, the Wagner-Traud hypothesis for electrochemical corrosion predicts that the corrosion potential will lie between the equilibrium

potentials for the anodic and cathodic partial reactions contributing to the overall corrosion reaction:

$$E^{a}_{eq} < E_{corr} < E^{c}_{eq} \quad (5)$$

Furthermore, the corrosion potential is predicted to lie closest to the equilibrium potential for the process with the highest exchange current density--that is, to the equilibrium potential for the "fastest" of the two partial processes. Exceptions to this last generalization do occur, particularly with passive systems, but nevertheless the generalization frequently serves as a convenient rule of thumb for the interpretation of corrosion processes.

Both theoretical calculations and experimental data indicate that the pH of the brine used in this work at 250°C lies within the range of 4.5 to 5.5.[2] A more exact estimate is not possible because of the complex nature of the brine, particularly with respect to the presence of ill-defined mineral buffering components. Nevertheless, the estimated value above is sufficiently precise to permit a meaningful comparison to be made between the observed corrosion potentials and cyclic voltammetric peak potentials, and the calculated equilibrium potentials as plotted in the potential-pH diagrams (Figs. 13-20). To aid the analysis presented below, we have plotted the corrosion potentials and the potentials of the principal oxidation and reduction peaks (see Table 3) as the hatched and cross-hatched areas, respectively, on the diagrams

for each element at 250°C. The ranges given for the corrosion potential correspond to those observed over the period of exposure of the alloys to the brine at the elevated temperature.

The corrosion potentials observed for carbon steel in high-salinity brine at 250°C straddle the region between the equilibrium lines for the formation of magnetite from iron and the reduction of hydrogen ion to form molecular hydrogen. Accordingly, the observed corrosion potential behavior is consistent (see Eq. 5) for the operation of these anodic and cathodic partial processes. Two of the observed oxidation peaks occur at potentials that are more positive than that for the Fe_3O_4/Fe couple, but they lie on the negative side of the equilibrium line for the Fe_2O_3/Fe_3O_4 couple. These peak potentials are also more positive than the extrapolated lines for the Fe^{2+}/Fe and $Fe(OH)^{+}/Fe$ couples in the pH region of interest as required by Eq. (2) for viable anodic processes. Accordingly, we tentatively attribute these two peaks to dissolution and film formation phenomena. The third clearly defined anodic peak occurs at a potential that is slightly positive to the Fe_2O_3/Fe_3O_4 equilibrium line (Fig. 14), and it may arise from the oxidation of magnetite (or iron) to an Fe(III) surface oxide phase.

Only one clearly defined reduction peak was observed when the potential was swept in the noble-to-active direction (Fig. 3). This peak lies just on the negative side of the Fe_3O_4/Fe equilibrium line,

and therefore satisfies Eq. (3) for the reduction of magnetite to iron. The general consistency of the arguments presented above is also supported by the experimental data for the "film-free" pseudo-corrosion potential, E_{ff}. Thus, prior sweeping of the potential to a highly active value (-1.06 V vs. SHE) is expected to reduce the surface oxide films back to metallic iron. The current on the reverse sweep (i.e., active-to-noble direction) is expected to be zero when the anodic current due to the dissolution of the metal or due to the formation of a thin film of magnetite balances that due to hydrogen evolution. Since the potential drop across any film formed under these conditions is expected to be less than that across the massive corrosion film that forms under freshly corroding conditions, it is expected that E_{ff} will more closely reflect the equilibrium potential of the anodic partial reaction than does E_{corr}. The observed close agreement between E_{ff} and equilibrium potentials for the Fe_3O_4/Fe, Fe^{2+}/Fe, or $Fe(OH)^{+}/Fe$ couples is in keeping with this expectation. Finally, the overpotentials for the oxidation and reduction peaks (i.e., $E_p - E_{eq}$) are quite small for carbon steel in the high salinity sulfide-free brine at 250°C compared with those observed for the other alloys (see Figs. 16, 18, and 20). The low overpotentials suggest that the charge transfer reactions (dissolution, oxidation, reduction) involving carbon steel are much faster (i.e., higher exchange current densities) than those for the other alloys studied in this work. This hypothesis is supported by the much higher corrosion rate for carbon steel compared with the other alloys in this high temperature geothermal brine.[2,15]

The other alloys that consist of essentially one component are titanium 50A and TiCode 12 (Table 2). Figure 20 shows a comparison of the corrosion potential and the oxidation and reduction peak potentials for these alloys with the calculated equilibrium potentials for titanium in sulfide-free high-salinity brine at 250°C. The free corrosion potential is found to straddle the equilibrium line for hydrogen evolution and lies within the stability region for rutile (TiO_2). Even if a much lower hydrogen fugacity than the 1 atm used for the calculations is assumed (e.g., 10^{-4} atm), the corrosion potential still lies within a few tenths of a volt below the hydrogen evolution line. In view of the highly resistive nature of the corrosion product films on titanium alloys in brine,[2] we suggest that E_{corr} is determined principally by the H^+/H_2 couple; that is, the alloys tend to act as hydrogen electrodes in high salinity brine at 250 C. This clearly implies that the exchange current density for the hydrogen evolution reaction is much greater than that for the formation of an oxide on the surface, as expected.

The observed oxidation peak potentials for titanium 50 A and TiCode 12 do not correlate well with any of the equilibrium lines for the phases chosen for construction of the titanium potential-pH diagram. Although Eq. (2) is satisfied, it is difficult to reconcile the large number of anodic peaks observed with the relative simplicity of the potential-pH diagram. It is possible that the peaks arise from redox processes that involve electroactive components of the brine or, more

likely, from localized dissolution-repassivation phenomena at the surface. This latter hypothesis is consistent with the frequently observed (see Figs. 11 and 12, third cycle), current fluctuations that occur when the potential is swept in both directions between 0 V and 1.0 V versus SHE (250°C). The localized dissolution sites apparently were not sufficiently stable to produce macroscopic pitting.[2,15]

It is more difficult to compare the kinetic behavior and the predicted thermodynamic properties for those alloys that do not contain a large excess of one component. Thus, for the stainless steels (E-Brite 26-1, 316L, Haynes Alloy 20 Mod, and Carpenter 20 Cb-3), all of which contain iron as the principal component, but also contain large amounts of chromium and nickel (except E-Brite 26-1, see Table 2), the corrosion potential tends to be more positive than that observed for carbon steel. In these cases, the E_{corr} values tend to correlate with equilibrium lines in the nickel diagram [e.g., $Ni(OH)^{+}/Ni$, NiO/Ni in Fig. 16] and also lie in the stability region for chromic oxide (Cr_2O_3) in the chromium-brine diagram (Fig. 18). This clearly demonstrates the influence of minor components on the corrosion behavior of Fe-Ni-Cr alloys, and also illustrates the difficulties inherent in using the potential-pH diagram for only the major component when analyzing the corrosion behavior of an alloy. The same general considerations apply to the nickel-based alloys (Inconel Alloy 625, Hastelloy Alloy G, and Hastelloy Alloy C-276--see Table 2). In these cases, however, there appears to be a much better

correlation between E_{corr} and equilibrium lines in the nickel -brine diagram (Fig. 16).

The difficulties outlined above for the interpretation of corrosion potentials for high alloy systems also apply when attempts are made to rationalize the cyclic voltammetric peak potentials and the E_{ff} values in terms of the potential-pH diagrams for the component metals. Thus, for the nickel-based alloys, E_{ff} is more negative than the lowest-lying equilibrium line in the nickel-brine diagram (Fig. 16), and therefore is not consistent with Eq. (5) for processes that involve phases containing nickel only. Instead, the E_{ff} values for these alloys (and for the stainless steels) appear to correlate much better with processes that involve phases containing chromium (Fig. 18); this suggests that the initial process that occurs on the surface of an Fe-Ni-Cr alloy is the dissolution of chromium from the matrix to form Cr^{2+} in solution or to form a thin Cr_2O_3 (or possibly chromium-containing spinel) layer on the surface. Likewise, many of the anodic peaks observed by cyclic voltammetry for nickel-based alloys lie below the equilibrium lines for reactions that involve phases containing nickel only (Fig. 16). These peak potentials are therefore in conflict with Eq. (2) if it is assumed that the peaks arise from oxidation of the nickel component of the alloys. The same consideration also applies to the stainless steels (Table 3), where some of the anodic peaks lie below all of the equilibrium lines in both the iron-brine and nickel-brine diagrams. In these cases, Eq. (2)

is satisfied only if it is assumed that the peaks arise from oxidation of the chromium component of the alloy. Thus, chromium appears to play a major role in determining the electrochemical, and hence corrosion behavior of Fe-Ni-Cr alloys in sulfide-free high salinity brine at elevated temperatures.

Potential-pH Diagrams for Sulfide-Containing Systems

Although few systematic studies of corrosion phenomena in sulfide-containing brines have been reported, the presence of dissolved sulfide is expected to exert a major influence over the corrosion behavior of metals and alloys in high temperature geothermal systems. In anticipation of future work in this field, we discuss here potential-pH diagrams[4] for iron and nickel in sulfide-containing ($[H_2S] + [HS^-] + [S^{2-}] = 10$ ppm) high salinity brine at 25°C and 250°C (Figs 21-24).

A total constant sulfide concentration has been assumed in the derivation of the diagrams. This constraint results in nonlinear potential-pH relationships for those reactions that involve solid sulfide phases and dissolved sulfide species (e.g., lines 5 and 11, Fig. 21), as previously shown.[4] Because the total sulfide content in a closed system is fixed, we considered that this constraint was reasonably realistic for the present purpose. Other constraints can be used for the derivation of potential-pH diagrams for complex systems. For example, Macdonald and Hyne[20] employed a constant H_2S partial pressure constraint

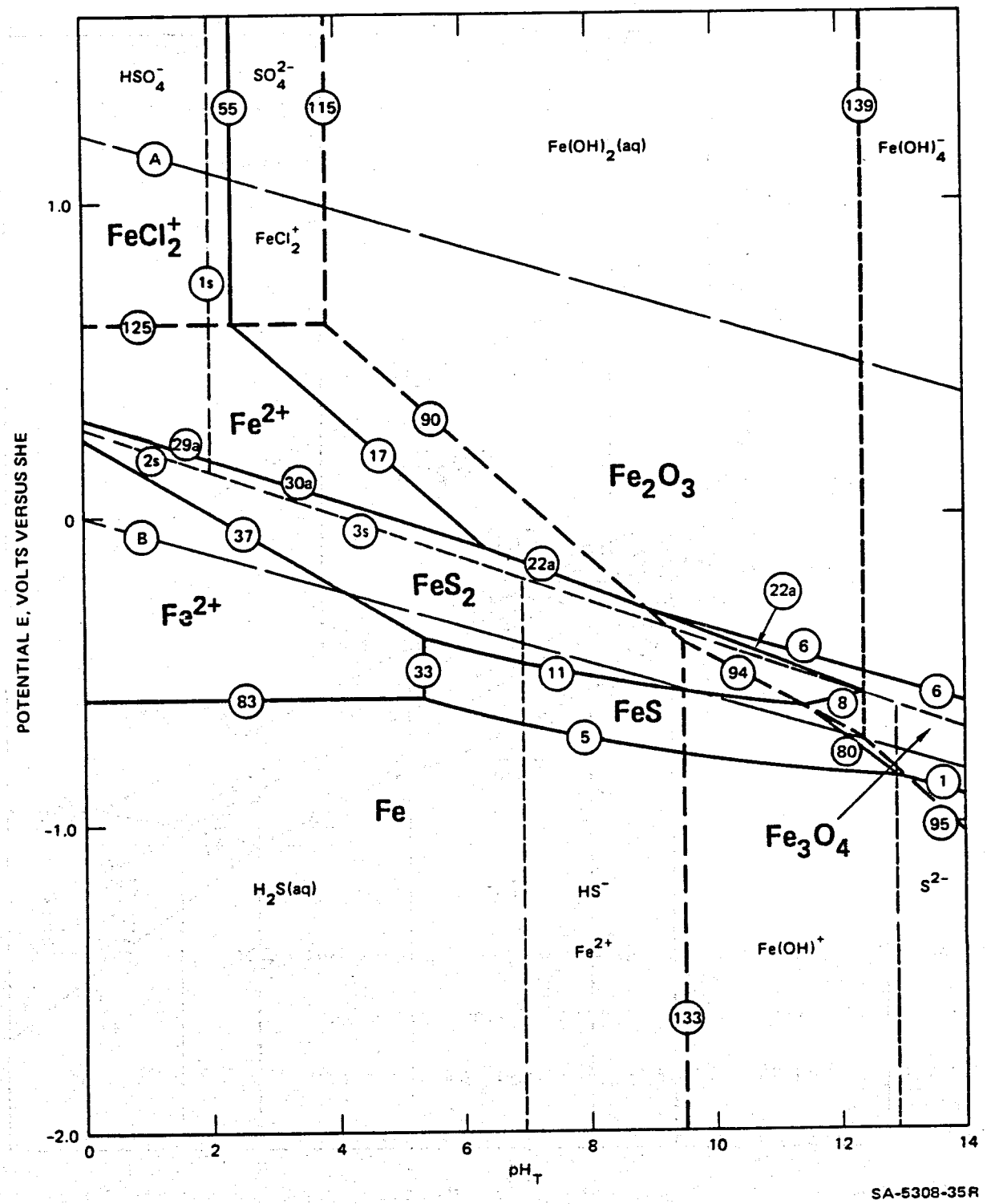

FIGURE 21 POTENTIAL-pH DIAGRAM FOR IRON IN HIGH-SALINITY BRINE AT 25°C IN THE PRESENCE OF 10 ppm TOTAL DISSOLVED SULFIDE ($H_2S + HS^- + S^{2-}$)

Activities of HSO_4^- and SO_4^{2-} = 10^{-6} molal. Activities of dissolved iron species = 10^{-4} molal.

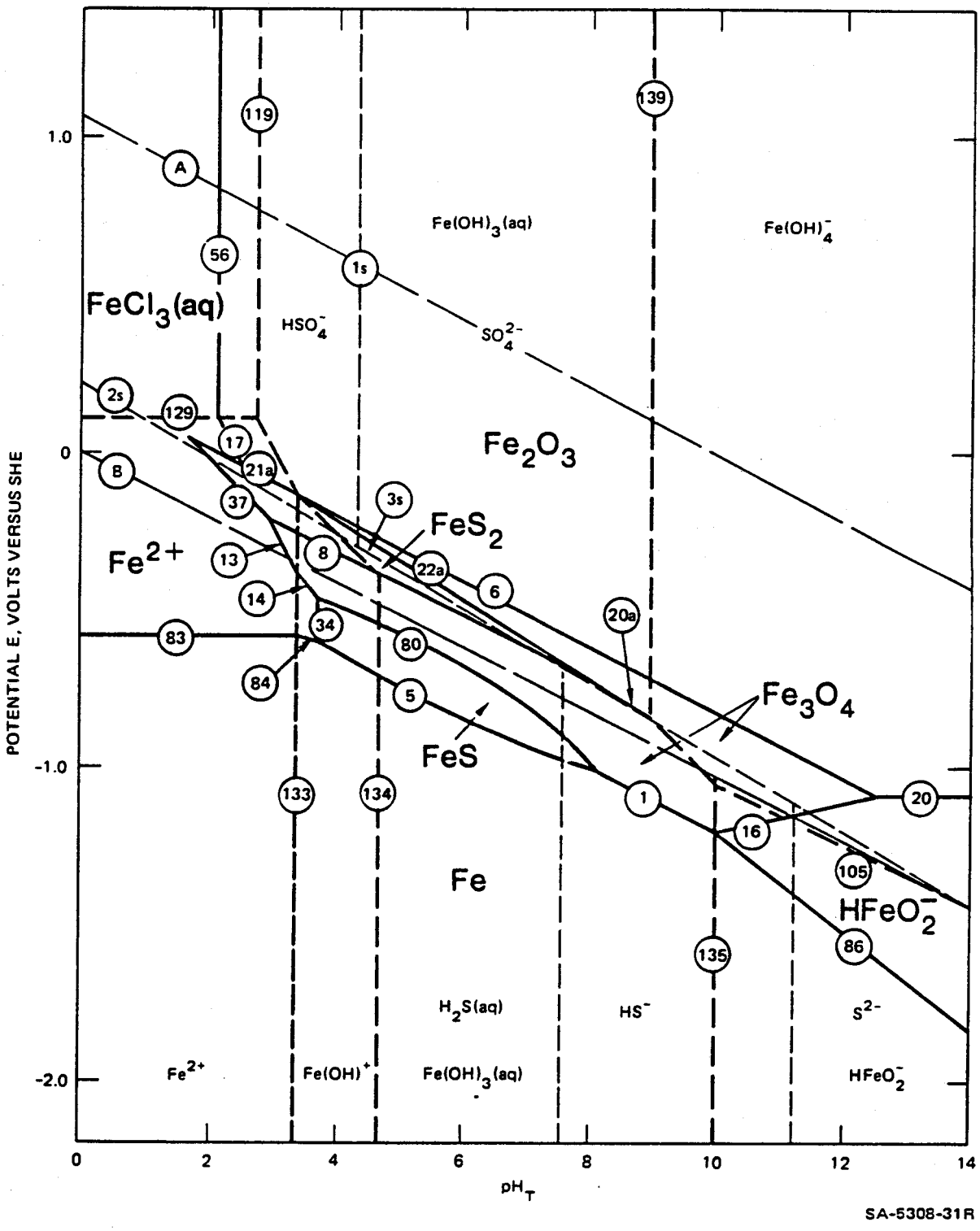

FIGURE 22 POTENTIAL-pH DIAGRAM FOR IRON IN HIGH-SALINITY BRINE AT 250°C IN THE PRESENCE OF 10 ppm TOTAL DISSOLVED SULFIDE ($H_2S + HS^- + S^{2-}$)

Activities of HSO_4^- and SO_4^{2-} = 10^{-6} molal. Activities of dissolved iron species = 10^{-4} molal.

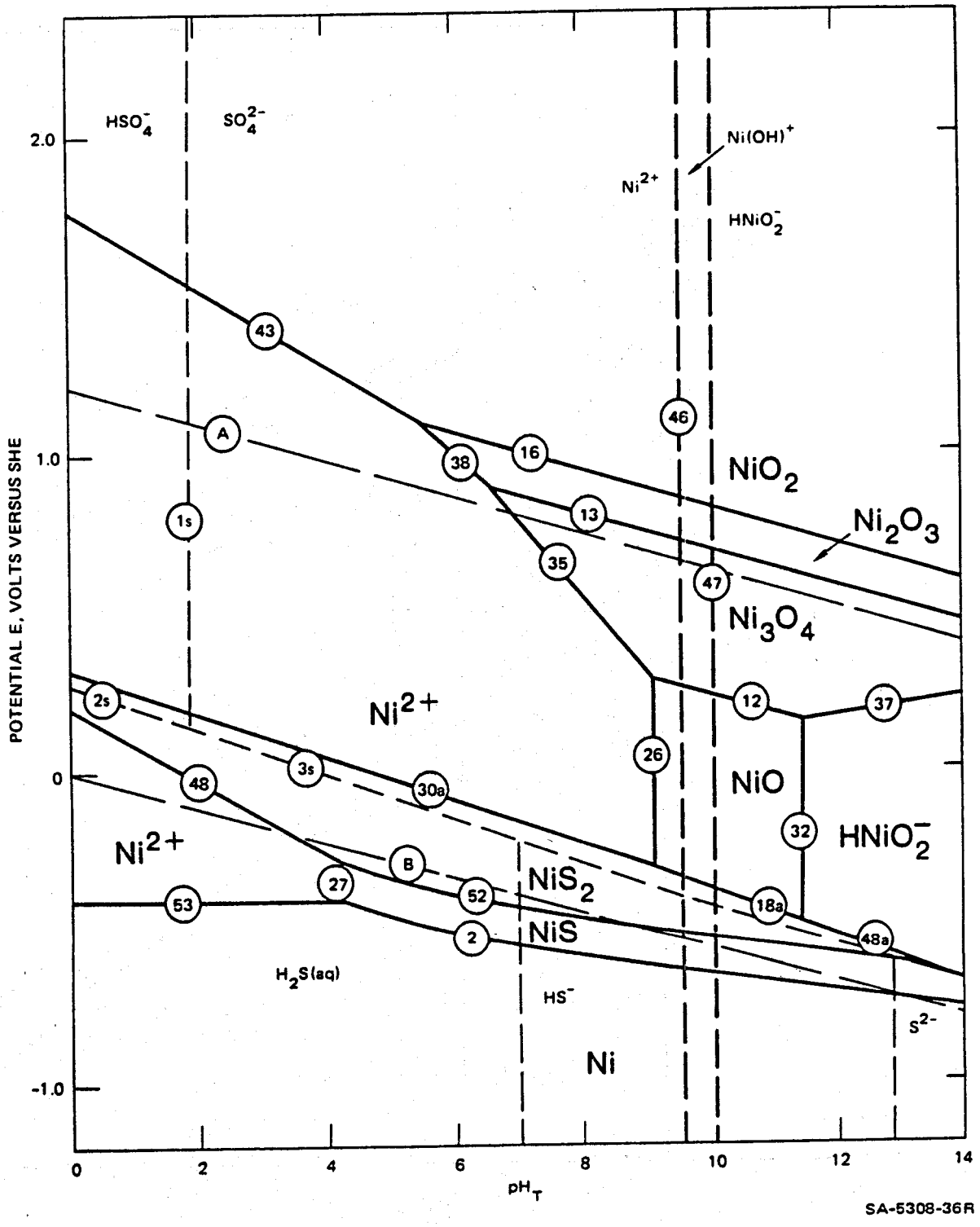

FIGURE 23 POTENTIAL-pH DIAGRAM FOR NICKEL IN HIGH-SALINITY BRINE AT 25°C IN THE PRESENCE OF 10 ppm TOTAL DISSOLVED SULFIDE ($H_2S + HS^- + S^{2-}$)
Activities of HSO_4^-, SO_4^{2-}, and dissolved nickel species = 10^{-6} molal.

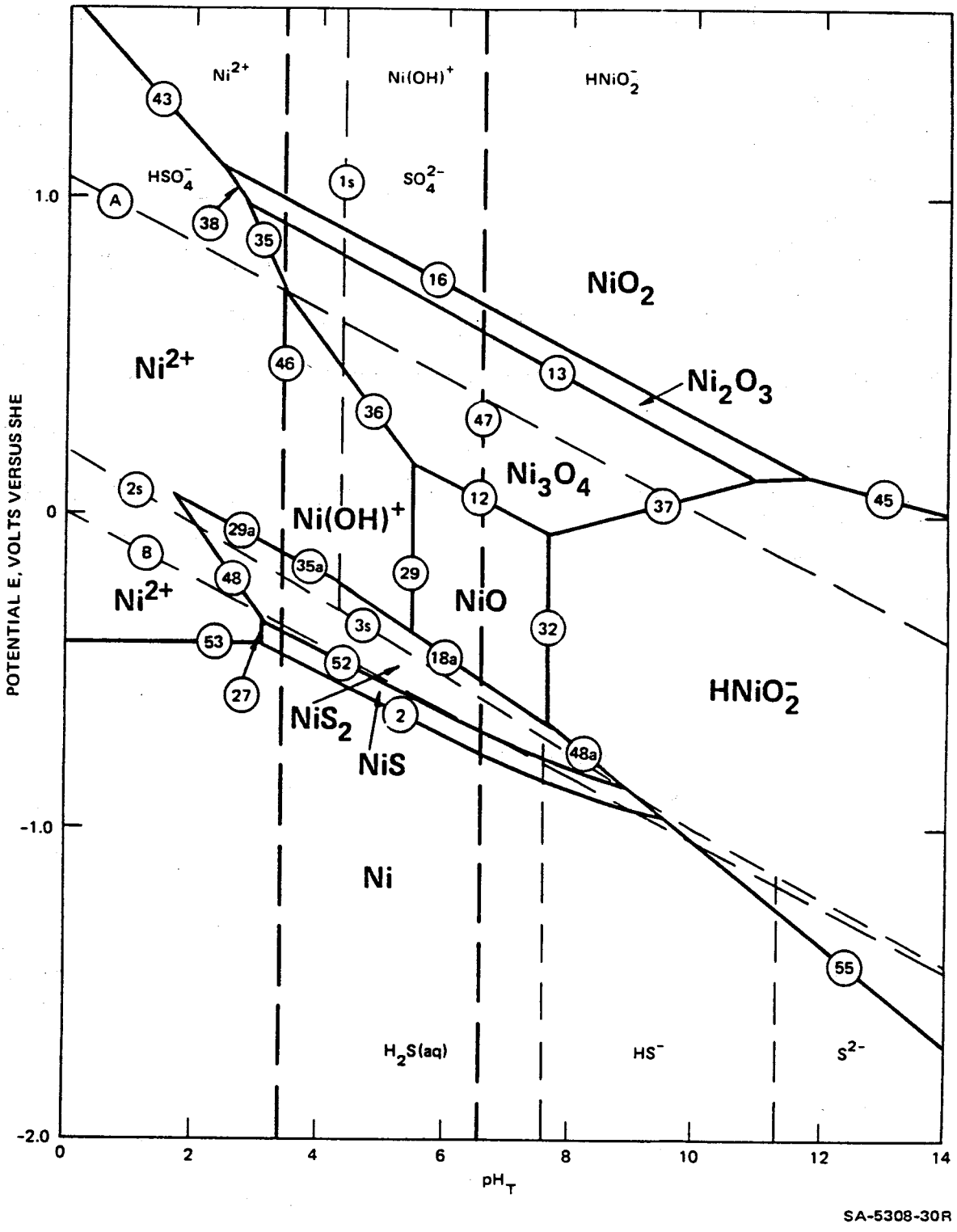

FIGURE 24 POTENTIAL-pH DIAGRAM FOR NICKEL IN HIGH-SALINITY BRINE AT 250°C IN THE PRESENCE OF 10 ppm TOTAL DISSOLVED SULFIDE ($H_2S + HS^- + S^{2-}$)

Activities of HSO_4^-, SO_4^{2-}, and dissolved nickel species = 10^{-6} molal.

in their thermodynamic analyses of the $Fe/H_2S/H_2O$ system at elevated temperatures as related to the production of heavy water (deuterium oxide) by the Girdler-Sulfide process.

Also plotted in Figs 21-24 are the potential-pH diagrams for the sulfur-water system, whose equilibrium relationships are designated by the light broken lines and by number ending with the letters (1s, 2s, etc). The sulfur-water equilibria are used to define the regions of predominance of various dissolved sulfide and sulfur oxyanion species which are subsequently employed for constructing the potential-pH diagrams for the metal/H_2S/H_2O systems. Elemental sulfur and dissolved polysulfide species were not considered in the present work, although they were taken into account in the more detailed analysis by Macdonald and Hyne[20] of the $Fe/H_2S/H_2O$ system. Because sulfur-containing species are present in the system of interest at very low concentrations, we do not believe that omission of elemental sulfur and the polysulfide ions materially affects the structure of the diagrams. All four diagrams were derived for constant activities for HSO_4^- and SO_4^{2-} equal to 10^{-4} m. In the case of the iron-brine system, the activities of dissolved metal-containing species were arbitrarily set equal to 10^{-4} m, whereas for the nickel-brine system dissolved species activities of 10^{-6} m were assumed. The higher activities for the iron-brine system were required so as to exceed the calculated minimum solubilities of the oxide phases at

elevated temperatures. Had the lower activity been assumed, the oxide phases would not have appeared as stable phases on the diagrams.[2]

In the case of both iron and nickel at 25°C, the most stable solid oxidation phase is the M(II) sulfide. Only troilite (stoichiometric FeS) was considered in the derivation of the diagram for iron, although it is recognized that other sulfide phases such as mackinawite ($Fe_{1+x}S$) and pyrrhotite (FeS_{1+x}) exist, and indeed mackinawite may form at lower potentials than troilite under certain conditions.[20] As the potential is increased, oxidation of MS to MS_2 is predicted to occur over almost the entire pH range. Note that Both FeS_2 and NiS_2 are Fe(II) and Ni(II) phases, respectively; the change in oxidation state is associated with the sulfur anions in the lattices. Thus FeS_2 and NiS_2 are best described as iron and nickel disulfides in which the average oxidation state of sulfur is -1. Note also that the conversion of MS to MS_2 involves reaction with H_2S (or its anions HS^- and S^{2-}) as shown by the location of the equilibrium lines 11 (Fig. 21) and 52 (Figs 23 and 24) in the stability region for sulfide (H_2S and HS^-) in the potential-pH diagram for the sulfur water system. On the other hand, equilibrium between MS_2 and the oxides Fe_3O_4, Fe_2O_3, and NiO involves sulfur oxyanions as demonstrated the potentials for these processes lying within the stability regions for HSO_4^- and SO_4^{2-}.

Increasing the temperature from 25°C to 250°C proved to have several important consequences for the thermodynamic equilibrium behavior of iron, nickel, and sulfur in sulfide-containing geothermal brine. Thus, the stable iron III complex at 25°C ($FeCl_2^+$) is no longer the predominant species at 250°C; the decrease in the dielectric constant of the medium favors the formation of the neutral complex $FeCl_3$ as previously noted in this paper. Similarly, pK_a for the dissociation of bisulfate ion (HSO_4^-) increases from approximately 1.98 at 25°C to 4.39 at 250°C. Increasing the temperature also has a marked effect on the stability regions for the dissolved metal-containing ions in geothermal brine. For example, as noted previously for the sulfide-free systems, the stability regions for cations at low pH values become more restricted as the temperature increases, whereas those for the anions $HFeO_2^-$ and $HNiO_2^-$ [or equivalently $Fe(OH)_3^-$ and $Ni(OH)_3^-$, respectively] increase. In the case of the anions the shifts in the lines for equilibrium between the ions and the oxides (e.g., line 32, Fig. 23) appear to be greater than can be accounted for by the change in the dissociation constant of water alone.[16-19] This observation suggests that the anions become stabilized with respect to the cations at elevated temperatures.

Probably the most important change in the diagrams for the $Fe/H_2S/H_2O/Cl^-$ and $Ni/H_2S/H_2O/Cl^-$ systems due to increasing temperature occurs in the relative stabilities of the sulfides and oxides. Thus, in both cases the disulfides, FeS_2 and NiS_2 are predicted to exhibit domains of

stability at 25°C that extend to very low pH values into the cation stability regions. The lower boundaries of these regions are determined by equilibrium between MS_2 and dissolved M^{2+} and H_2S, whereas the upper boundaries represent equilibrium between MS_2 and dissolved M^{2+} and the oxyanions HSO_4^- or SO_4^{2-}. Thus, if the potential is first increased from within the lower stability region for M^{2+}, at some point the formation of solid FeS_2 (line 37, Fig. 21) or NiS_2 (line 48, Fig. 23) becomes spontaneous by oxidative deposition. However, if the potential is increased still further, oxidative dissolution of the disulfides can occur. These relationships are of considerable importance in the mining and geothermal industries because they provide the thermodynamic boundaries for the oxidative and reductive dissolution of pyrite ores (for example) and pyrite-rich scales in geothermal systems. At elevated temperatures, however, the stability domains for the sulfides, and particularly for the disulfides FeS_2 and NiS_2, are reduced sharply in size, thereby indicating much more restrictive conditions for the formation of these phases in high-temperature geothermal systems. Nevertheless, Seward[25] has argued that the down-hole redox potential and pH in the Broadlands geothermal field south of Reporoa in New Zealand lie within the stability region for FeS_2, and indeed pyrite is observed in core samples from the steam-producing formation.

SUMMARY

The use of potential-pH diagrams for the interpretation of corrosion phenomena in geothermal bines has been discussed. Although considerable care must be exercised when comparing kinetic parameters with equilibrium properties, we have shown that the diagrams are valuable for the rationalization of corrosion phenomena in terms of proposed partial anodic and cathodic reactions. Furthermore, the diagrams conveniently summarize the equilibrium properties of metal-brine systems in general, and are therefore of considerable value for the interpretation of non-corrosion processes such as scaling.

ACKNOWLEDGMENTS

Financial support of this work by NSF(RANN) under Grant No. AER 76-00713 is gratefully acknowledged.

REFERENCES

1. J. F. Carter and F. X. McCawley, J. Metals, 30, 11 (1978).

2. B. C. Syrett, D. D. Macdonald, H. Shih, and S. S. Wing, "Corrosion Chemistry of Geothermal Brines. Part 1: Low Salinity Brines, Part 2: High Salinity Brine," Final report to NSF(RANN) and Dept. of Energy, Washington, D.C. NSF(RANN) Grant No. AER 76-00713 (1977).

3. D. D. Macdonald and B. C. Syrett, "The Use of Potential-pH Diagrams for the Interpretation of Corrosion Phenomena in High Salinity Geothermal Brines," Corrosion, in press (1978).

4. D. D. Macdonald and B. C. Syrett, "Potential-pH Diagrams for Iron and Nickel in High Salinity Geothermal Brine Containing Low Levels of Hydrogen Sulfide," Corrosion, Submitted for publication (1978).

5. D. D. Macdonald, Transient Techniques in Electrochemistry, Plenum Press, New York (197).

6. D. D. Macdonald and D. Owen, In High Temperature High Pressure Electrochemistry in Aqueous Solutions, Ed. by R. W. Staehle, D. de G. Jones, and J. E. Slater, NACE-4, Houston, Texas (1976), p. 513.

7. R. L. Cowan and R. W. Staehle, J. Electrochem. Soc., Vol. 118, p. 557 (1971).

8. D. D. Macdonald, in Modern Aspects of Electrochemistry, Ed. by J. O'M. Brockris and B. E. Conway, Vol. 11, Plenum Press, New York (1975), p. 141.

9. D. D. Macdonald, Corrosion, Vol. 34, p. 75 (1978).

10. D. D. Macdonald, P. Butler, and D. Owen, Can. J. Chem., Vol. 51, p. 2590 (1973).

11. D. D. Macdonald and D. Owen, J. Electrochem. Soc., Vol. 120 p. 317 (1973).

12 J. Postlethwaite, Electrochim. Acta, Vol. 12, p. 337 (1962).

13. D. de Jones and R. W. Staehle, eds., High Temperature High Pressure Electrochemistry in Aqueous Solutions, NACE-4, Houston, Texas (1976).

14. D. D. Macdonald and B. Roberts, Electrochim. Acta, Vol. 23, p. 781 (1978).

15. B. C. Syrett, D. D. Macdonald, H. Shih, and S. S. Wing, to be published.

16. D. D. Macdonald, G. Shierman, and P. Butler, "The Thermodynamics of Metal-Water Systems at Elevated Temperatures. I The Water and Copper-Water Systems," Atomic Energy of Canada Ltd. report, AECL-4136 (1972).

17. D. D. Macdonald, G. Shierman, and P. Butler, "The Thermodynamics of Metal-Water Systems at Elevated Temperatures II The Iron-Water System," Atomic Energy of Canada, Ltd. report, AECL-4137 (1972).

18. D. D. Macdonald, G. Shierman, and P. Butler, "The Thermodynamics of Metal-Water Systems at Elevated Temperatures. III The Cobalt-Water System," Atomic Energy of Canada Ltd. report, AECL-4138 (1972).

19. D. D. Macdonald, "The Thermodynamics of Metal-Water Systems at Elevated Temperatures. IV. The Nickel-Water System," Atomic Energy of Canada Ltd. report, AECL-4139 (1972).

20. D. D. Macdonald and J. B. Hyne, "The Thermodynamics of the Iron/Sulfur/Water System," Final report to Atomic Energy of Canada Ltd., Pinawa, Manitoba (1976).

21. G. B. Naumov, B. N. Ryzhenko, and I. L. Khodakovsky, Handbook of Thermodynamic Data, Transl. U.S. Geological Survey USGS-WRD-74-001 (1974).

22. D. G. Taylor, "Thermodynamic Properties of Metal-Water Systems at Elevated Temperatures," Report No. 77CRD213, General Electric Co., Schenectady, New York (1977).

23. R. E. Mesmer and C. F. Baes, Inorg. Chem., Vol. 10, p. 2290 (1971).

24. D. D. Macdonald, P. Butler, and D. Owen, J. Phys. Chem., Vol. 77. p. 2474 (1973).

25. T. M. Seward, Am. J. Sci., Vol. 274, 190 (1974).